HOW DO GALAXIES TRACE A LARGE SCALE STRUCTURE?:
A CASE STUDY AROUND A MASSIVE PROTOCLUSTER AT $Z = 3.13$

Ke Shi[1], Yun Huang[1], Kyoung-Soo Lee[1,2], Jun Toshikawa[3], Kathryn N. Bowen[1], Nicola Malavasi[4],
B. C. Lemaux[5,8], Olga Cucciati[6,7], Olivier Le Fevre[8], Arjun Dey[9]

ABSTRACT

In the hierarchical theory of galaxy formation, a galaxy overdensity is a hallmark of a massive cosmic structure. However, it is less well understood how different types of galaxies trace the underlying large-scale structure. Motivated by the discovery of a $z = 3.13$ protocluster, we examine how the same structure is populated by Lyα-emitting galaxies (LAEs). To this end, we have undertaken a deep narrow-band imaging survey sampling Lyα emission at this redshift. Of the 93 LAE candidates within a $36'\times36'$ (70×70 Mpc^2) field, 21 galaxies form a significant surface overdensity ($\delta_{\Sigma,\mathrm{LAE}} = 3.3 \pm 0.9$), which is spatially segregated from the Lyman break galaxy (LBG) overdensity. One possible interpretation is that they trace two separate structures of comparable masses ($\approx 10^{15} M_\odot$) where the latter is hosted by a halo assembled at an earlier time. We speculate that the dearth of LAEs in the LBG overdensity region may signal the role of halo assembly bias in galaxy formation, which would suggest that different search techniques may be biased accordingly to the formation age or dynamical state of the host halo. The median Lyα- and UV luminosity is 30–70% higher for the protocluster LAEs relative to the field. This difference cannot be explained by the galaxy overdensity alone, and may require a top-heavy mass function, higher star formation efficiency for protocluster halos, or suppression of galaxy formation in low-mass halos. A luminous Lyα blob and an ultramassive galaxy found in this region paint a picture consistent with the expected early growth of galaxies in clusters.

1. INTRODUCTION

In the hierarchical theory of structure formation, initial small density fluctuations give rise to the formation of first stars and galaxies. These structures subsequently grow larger and more massive via mergers and accretion (White & Rees 1978). In this context, galaxy clusters provide unique laboratories to study how galaxy formation proceeded in the densest cosmic structures. In the local universe, cluster galaxies form a tight 'red sequence' (Visvanathan & Sandage 1977; Bower et al. 1992) and obey the 'morphology-density' relation (Dressler 1980; Goto et al. 2003), showcasing the impact of dense environments on the star formation activities of the inhabitants. In addition, existing studies strongly suggest that cluster galaxies experienced early growth at an accelerated pace followed by swift shutdown of their

star formation, and have been evolving passively in the last ≈ 10 Gyr (e.g., Steidel et al. 2005; Eisenhardt et al. 2008; Hatch et al. 2011; Koyama et al. 2013; Cooke et al. 2014; Husband et al. 2016; Shimakawa et al. 2018).

The presence of massive quiescent galaxies in clusters out to $z \sim 1$ argues that the negative impact of dense environments must become less pervasive at earlier times, and that the star formation-density relation may even reverse (e.g., Elbaz et al. 2007; Cooper et al. 2008; Tran et al. 2010; Koyama et al. 2013; Brodwin et al. 2013; Alberts et al. 2014; Santos et al. 2014; Welikala et al. 2016) although it is still a matter of debate when this reversal occurs (e.g., see Lemaux et al. 2018b). While the enhanced level of star formation activity in young forming clusters would certainly be consistent with the general expectations of cluster formation, direct evidence of this observational picture needs to come from distant galaxies residing in 'protoclusters' at $z > 2$, the epoch in which much of star formation activity and subsequent quenching are expected to have occurred.

Young protoclusters are far from virialized, and are distributed over large cosmic volumes with their angular sizes expected to span $10'–30'$ in the sky (e.g., Chiang et al. 2013; Muldrew et al. 2015). Moreover, the largest structures (those which will evolve into systems similar to Coma with their final masses exceeding $\gtrsim 10^{15} M_\odot$) are extremely rare with a comoving space density of $\approx 2\times10^{-7}$ Mpc^{-3} (Chiang et al. 2013). Combined with their optical faintness, these characteristics make it observationally challenging to robustly identify protoclusters, and to conduct a complete census of their constituents for those confirmed.

Nevertheless, some protoclusters have been confirmed thanks to deep extensive spectroscopy of 'blank fields'

[1] Department of Physics and Astronomy, Purdue University, 525 Northwestern Avenue, West Lafayette, IN 47907
[2] Visiting astronomer, Kitt Peak National Observatory (KPNO), National Optical Astronomy Observatory, which is operated by the Association of Universities for Research in Astronomy (AURA) under a cooperative agreement with the National Science Foundation.
[3] Institute for Cosmic Ray Research, the University of Tokyo, ICRR, 5-1-5 Kashiwanoha, Kashiwa, 277-0882 Japan.
[4] Institut d'Astrophysique Spatiale, CNRS (UMR 8617), Université Paris-Sud, Bâtiment 121, Orsay, France.
[5] Department of Physics, University of California, Davis, One Shields Ave., Davis, CA 95616.
[6] INAF–Osservatorio Astronomico di Bologna, via Gobetti, 93/3, I-40129, Bologna, Italy.
[7] University of Bologna, Department of Physics and Astronomy (DIFA), V.le Berti Pichat, 6/2 - 40127, Bologna, Italy.
[8] Aix Marseille Université, CNRS, LAM (Laboratoire d'Astrophysique de Marseille) UMR 7326, 13388, Marseille, France.
[9] National Optical Astronomy Observatory, Tucson, AZ 85726.

(e.g., Steidel et al. 1998, 2000, 2005; Cucciati et al. 2014; Lee et al. 2014; Dey et al. 2016a; Lemaux et al. 2014; Wang et al. 2016; Cucciati et al. 2018; Jiang et al. 2018), which give us a glimpse of diverse galaxy types residing in protoclusters, such as luminous Lyα nebulae, dusty star-forming galaxies, and massive and quiescent galaxies. Studying these galaxies in details will ultimately lead us to a deeper understanding of how cluster elliptical galaxies and the brightest cluster galaxy (BCG) are assembled.

Another critical avenue in understanding cluster formation is a detailed characterization of their large-scale environments. Such information will pave the way to understand how galaxies' star formation activity is linked to their immediate local density. One efficient way to do so is to pre-select candidate galaxies in overdense regions photometrically and follow them up with spectroscopy. Given the expected high star formation activity, a selection of star-forming galaxies (such as Lyman break galaxies; LBGs hereafter) can provide a reasonable candidate pool, albeit not a complete one (e.g., Toshikawa et al. 2012; Lee et al. 2014; Dey et al. 2016a; Toshikawa et al. 2016, 2018), from which possible overdense structures may reveal themselves as higher surface density regions (Chiang et al. 2013). Alternatively, a narrow-band imaging selection sampling strong emission lines such as Lyα or Hα has emerged as a popular choice as it allows sampling of a small slice of cosmic volume. Such emission-line based selection methods are advantageous in defining environments with minimal contamination from fore- and background interlopers (e.g., Pentericci et al. 2000; Venemans et al. 2007; Overzier et al. 2008; Kuiper et al. 2011; Hatch et al. 2011; Mawatari et al. 2012; Cooke et al. 2014; Yang et al. 2010; Bădescu et al. 2017; Higuchi et al. 2018).

Given that a galaxy overdensity is a hallmark of massive cosmic structures, any method that is able to detect them should, in principle, serve us equally well in identifying progenitors of massive clusters provided that their galaxy biases are well understood. Understanding how different galaxy populations trace the underlying large-scale structure – not only LBGs and Lyα emitters (LAEs) but also other types such as AGN and dusty star-forming galaxies that have been reported to reside in abundance in dense protocluster environments – can illuminate the early stages of cluster elliptical formation, and also help us fine-tune the search techniques in the future in the era of wide-area surveys such as Large Synoptic Survey Telescope and Hobby-Eberly Dark Energy Experiment.

In this paper, we present a follow-up study of a galaxy overdensity in the D1 field of the Canada-France-Hawaii-Telescope Legacy Survey (CFHTLS). The structure 'D1UD01' was discovered as a result of a systematic search of protoclusters conducted by Toshikawa et al. (2016) where candidate structures were identified based on their prominent surface densities of LBGs at $z \sim 3 - 5$. Follow-up spectroscopy confirmed five galaxies at $z = 3.13$ located within 1 Mpc of one another, suggesting the possible existence of a highly overdense structure. At this redshift, Lyα emission is conveniently redshifted into a zero-redshift [O III] filter, providing us the unique opportunity to explore how line-emitting galaxies are popu-

lated in a massive structure identified and characterized by an independent method.

This paper is organized as follows. In § 2, we present the new narrow-band imaging of a subsection of the CFHTLS D1 field containing a confirmed protocluster at $z = 3.13$. Combining the new observations with existing broad-band data, we identify a sample of LBGs and LAEs, and conduct a search for Lyα nebulae in the field (§ 3). In § 4, we measure their angular distributions and identify possible overdensity regions. In § 5, we discuss the masses of their descendants, examine a possible trend of star formation activity with local environment, and speculate the implications based on these results. A search for a proto-BCG is also presented. Finally, a summary of our results is given in § 6.

We use the WMAP7 cosmology $(\Omega, \Omega_\Lambda, \sigma_8, h) = (0.27, 0.73, 0.8, 0.7)$ from Komatsu et al. (2011). Distance scales are given in comoving units unless noted otherwise. All magnitudes are given in the AB system (Oke & Gunn 1983). In the adopted cosmology, $1''$ corresponds to the angular scale of 7.84 kpc at $z = 3.13$.

2. DATA AND PHOTOMETRY

2.1. *New observations*

In September 2017, we obtain narrowband imaging of the protocluster candidate 'D1UD01' and the surrounding region in the D1 field, one of the four Canada-France-Hawaii-Telescope Legacy Survey deep fields. The pointing center is $[\alpha, \delta] = [36.316°, -4.493°]$. The data are taken with the Mosaic 3 Camera (Dey et al. 2016b) on the Mayall 4m telescope of the Kitt Peak National Observatory (NOAO Program ID: 2017B-0087). The KPNO Mosaic [O III] filter no. k1014 (*o3* filter, hereafter) is used, with a central wavelength of 5024.9Å and a full-width-at-half-maximum (FWHM) of 55.6Å. The *o3* filter samples redshifted Lyα line in the range $z = 3.132 \pm 0.023$, spanning a line-of-sight distance of 44 Mpc.

The individual exposure time of 1200 sec is used with small-offset dithers (`FILLGAP`) optimized to fill in CCD chip gaps. We discard the frames taken with seeing $> 1''.3$. We identify and remove a handful of frames which appear to have been taken when the guide star was temporarily lost, resulting in the sources to leave visible trails in the image. The total exposure time of the new imaging is 14.0 hr. The mosaic image has a native pixel scale of $0.25''$.

We calibrate the astrometry with the IRAF task `msccmatch` using the stars identified in the CFHTLS deep survey catalog (Gwyn 2012), and re-project each image with a pixel scale of $0''.186$ using the tangent point of the CFHTLS images. The relative intensity scale is determined using the IRAF task `mscimatch`. The reprojected frames are then combined into a final image stack using a weighted average, with the average weight inversely proportional to the variance of the sky noise measured in the reprojected frames. We trim the images removing the area near the edges with less than 20% of the maximum exposure time, and mask areas near bright saturated stars. The final mosaic has an effective area of 0.32 deg^2 with a measured seeing of $1''.2$.

As most of our observations were taken in non-photometric conditions, we calibrate the photometric zeropoint using the CFHTLS broad-band catalogs. The

TABLE 1
DATA SET

Band	Instrument	Limiting magnitude[a] (5σ,AB)	FWHM ($''$)
u	MegaCam/CFHT	27.50	0.8
g	MegaCam/CFHT	27.82	0.8
$o3$	Mosaic-3/Mayall	25.21	1.2
r	MegaCam/CFHT	27.61	0.8
i	MegaCam/CFHT	27.10	0.8
z	MegaCam/CFHT	26.30	0.8

[a] 5σ limiting magnitude measured in a 2$''$ diameter aperture.

central wavelength of the g band is 4750Å, reasonably close to that of the $o3$ filter at 5024.9Å. We define a sample of galaxies that have the g-band magnitude of 21–25 mag with the blue $g - r$ colors ($g - r \leq 0.2$), and determine the $o3$ band zeropoint such that the median $o3 - g$ color is zero. We further check our result by plotting the $g - r$ colors vs $o3 - g$ colors for all photometric sources. We confirm that the intercept in the $o3 - g$ colors is zero.

In conjunction with the new $o3$ data, we use the deep $ugriz$ images available from the CFHTLS Deep Survey (Gwyn 2012). The broad band images are trimmed to have the identical dimension to the $o3$-band data. The photometric depth (measured from the sky fluctuations by placing 2$''$ diameter apertures in random image positions) and native image quality of these bands are summarized in Table 1; their filter transmission curves are illustrated in Figure 1.
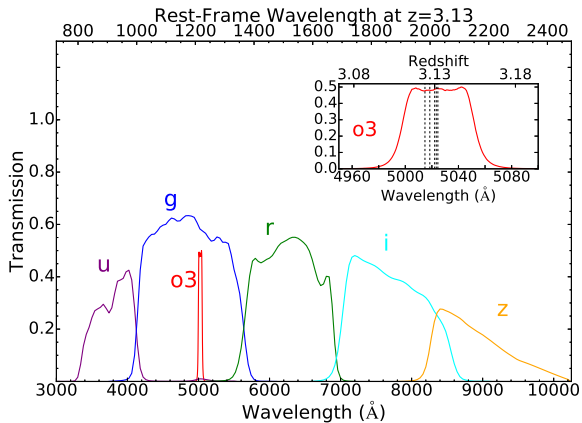

FIG. 1.— Total throughput (filter+mirror+optics+CCD response) of the filters used to identify Lyα emitters in this work. The rest-frame wavelength range at $z = 3.13$ is shown on the top axis. The inset zooms in on the $o3$ filter region. The corresponding redshift range of Lyα emission is indicated on top. The spectroscopic redshifts of the five confirmed members are indicated by dotted vertical lines.

2.2. Photometry

We create a multiwavelength photometric catalog as follows. First, we homogenize the PSFs of the broad-band data to match that of the worst-seeing data, i.e., the $o3$ image (FWHM=1.2$''$). The radial profile of the PSF in each image is approximated as a Moffat profile with the measured seeing FWHM, and a noiseless convolution kernel is derived using the IDL routine `MAX_ENTROPY`. The broad band data is then convolved with their respective

kernels to create a PSF-matched image.

We create the narrow band catalog by running the SExtractor software (Bertin & Arnouts 1996) in the dual image mode. The $o3$ band image is used for detection, while photometric measurements are performed in all the broad band images. The SExtractor parameter MAG_AUTO is used to estimate the total magnitude, while colors are computed from the fluxes within a fixed isophotal area (i.e., FLUX_ISO). As the images are PSF-matched, aperture correction in all bands is assumed to be given by the difference between MAG_AUTO and MAG_ISO estimated in the detection band. A total of 43,940 sources are detected in the $o3$ image. We also use the broad-band-only catalog released as part of the CFHTLS final data release[10] (referred to as a 'T0007' version, hereafter); the T0007 catalog contains 249,771 sources where a gri selected χ^2 is used as a detection image.

3. ANALYSIS

3.1. Lyα-emitting Galaxies at $z \sim 3.13$

The primary goal of this paper is to investigate the possible presence of a large scale structure in and around the five spectroscopic sources at $z = 3.13$ discovered by Toshikawa et al. (2016). The $o3$ filter is ideally suited for this task as redshifted Lyα emission falls into it at $z = 3.13 \pm 0.02$. The redshift selection function, converted from the filter transmission, is illustrated in the inset of Figure 1. The Lyα-based spectroscopic redshifts of the five galaxies confirmed by Toshikawa et al. (2016) are marked as vertical dashed lines.

We adopt the following criteria to select LAE candidates at $z = 3.13$:

$$o3 - g < -0.9 \quad \wedge \quad \mathrm{S/N}(o3) \geq 7$$
$$\wedge \; [\; u - g > 1.2 \quad \vee \quad \mathrm{S/N}(u) < 2\;] \qquad (1)$$

where the symbols $\vee$ and $\wedge$ are the logical "OR" and "AND" operators, respectively, and S/N denotes the signal-to-noise ratio within the isophotal area. The $u - g$ color criterion requires a strong continuum break falling between the two filters to ensure that the source lies at $z \gtrsim 2.7$.

To design the selection criteria, we synthesize the colors by generating model galaxies spanning a range of rest-frame UV continuum slope, Lyα emission line equivalent width (EW), and Lyα luminosity. The galaxy's spectral energy distribution (SED) is constructed assuming a constant star formation history observed at the population age of 100 Myr, with a Salpeter (1955) initial mass function and solar metallicity. We account for attenuation by intergalactic hydrogen using the H I opacity given by Madau (1995), and assume that the interstellar extinction obeys the Calzetti et al. (2000) reddening law.

To the reddened, redshifted galaxy SED, we add a Lyα emission with a Gaussian line profile centered at $1215.67(1 + z)$Å and an intrinsic line width of 3Å. The redshift $z = 3.13$ is assumed. Given that the $o3$ filter is much wider than the line width, exact values assumed for the line width are not important as long as they reproduce the observed galaxy colors and line FWHM reason-
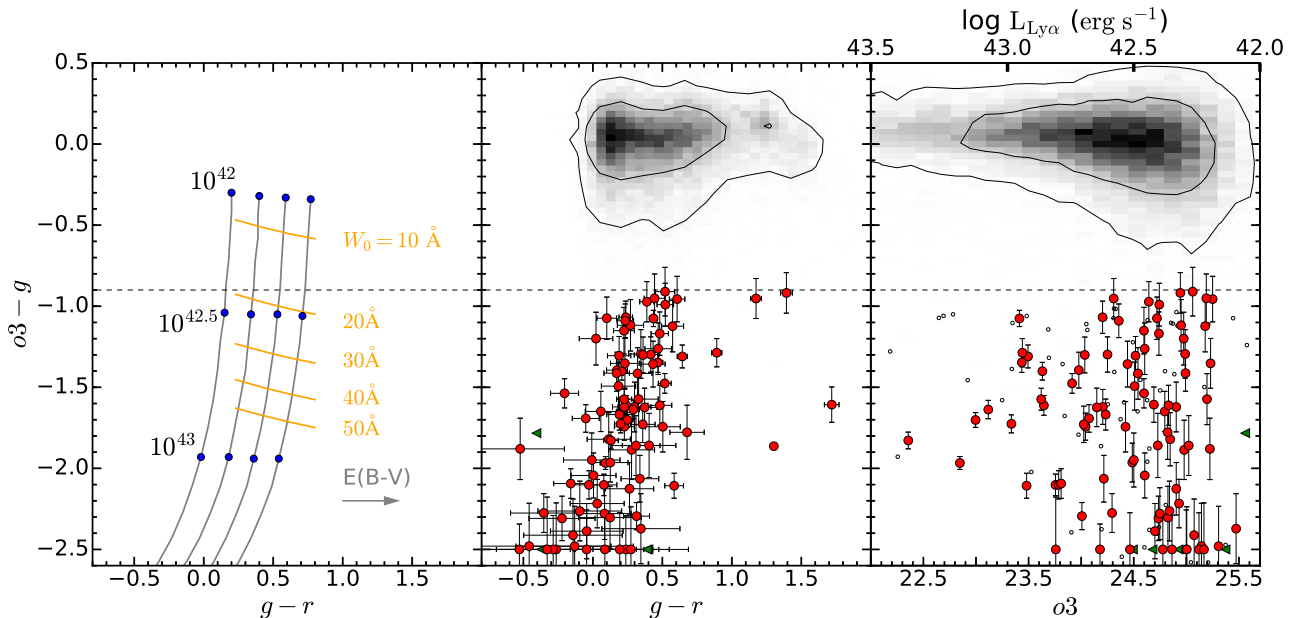
FIG. 2.— *Left:* Theoretical tracks for LAEs of different luminosities and dust reddening in the $o3 - g$ vs $g - r$ color diagram. The grey lines show the color evolution with increasing Lyα luminosities (from top to bottom) at four reddening values ($E(B - V) = 0 - 0.3$ in steps of 0.1 from left to right). Blue points show the Lyα luminosities, $10^{42.0}$, $10^{42.5}$ and $10^{43.0}$ erg s^{-1} at the continuum g band magnitude of 25.5. Orange lines represent the Lyα rest-frame equivalent widths (W_0) of 10, 20, 30, 40, and 50Å. The $o3 - g$ color cut (dashed horizontal line) approximately corresponds to $W_0 \gtrsim 20$Å. *Middle:* the color-color diagram for all $o3$ detected sources. The two contour lines enclose 68% and 95% of the sources. Galaxies that satisfy the LAE criteria are indicated as red circles; those undetected in g or r band are shown as green triangles. Galaxies with $o3 - g \leq -2.5$ are shown at the color position of -2.5. *Right:* $o3 - g$ color as a function of $o3$-band magnitude. Sources that do not meet the $u - g$ color cut are shown in open circles. The approximate Lyα luminosities corresponding to the $o3$ magnitude are indicated on the upper abscissa.

ably well. The Lyα limiting luminosity from the above criteria is $\approx 10^{42.3}$ erg s^{-1}. No extinction is applied to the Lyα line as it represents the observed luminosity.

In the left panel of Figure 2, we show the expected $o3 - g$ and $g - r$ colors for different reddening values with different line luminosities. For the Lyα luminosities indicated in the same panel, we assume a continuum g band magnitude of 25.5 mag, which is based on the median value of our LAE sample. Finally, we stress that our photometric criteria (Equation 1) are sensitive to the line equivalent width and redshifts of the source, but not to the choice of IMF and metallicity adopted to create the base galaxy SED. For example, if a sub-solar metallicity ($Z = 0.008$) is assumed, the $g - r$ colors would be bluer by 0.04 mag while the $o3 - g$ colors would remain unchanged.

The middle and right panel of Figure 2 show the color-color and color-magnitude distributions of the $o3$-detected sources. The adopted selection criteria (Equation 1) correspond to the rest-frame equivalent widths $\gtrsim 20$Å at the target redshift range, and result in 94 LAE candidates. Their $g - r$ colors suggest that the majority are consistent with being relatively dust-free with a few exceptions. The LAE candidates are distributed over a $\approx 4,365$ Mpc^2 (1156 arcmin^2) field. With the exception of six (green triangles in Fig 2), all have robust continuum detections in the g or r band.

Based on the photometric data, we derive the physical properties of our LAE candidates including the rest-frame Lyα EW (W_0), Lyα luminosity ($L_{\mathrm{Ly}\alpha}$), UV continuum luminosity at the rest-frame 1700Å (L_{1700}), and UV spectral slope (β: defined as $f_\lambda \propto \lambda^\beta$). The Ly$\alpha$ lu-

minosity and EW are derived following the prescription given in Xue et al. (2017), which fully takes into account the Lyα forest attenuation in the relevant filters. The UV slope is computed from a linear regression fitting of the riz photometric data; the continuum luminosity L_{1700} is then extrapolated from the i-band flux density assuming the slope β. These quantities are listed in Table 3.

Four galaxies in our LAE sample are significantly redder ($g - r > 1.0$) than the majority. We check them in the image to verify these sources are real and robust detections. One is likely an AGN with an extremely high UV luminosity ($r = 21.7$ mag) and a point-like morphology. The other three may be more dust reddened than the other 90 LAE candidates. Dusty LAEs are rare, but have been reported in the literature (Oteo et al. 2012; Bridge et al. 2013), some of which are IR-luminous galaxies detected in mid-infrared surveys. Assuming the Calzetti et al. (2000) dust law, their UV slope β values correspond to the color excess of the stellar continuum $E(B - V)$ of 0.20, 0.16, and 0.23, respectively, compared to the median value of 0.10 for the full LAE sample. These values are comparable to those measured for dusty LAEs with *Herschel*/PACS detection studied by Oteo et al. (2012).

Three of the five spectroscopic sources in the 'D1UD01' structure satisfy our LAE selection; their IDs in the Toshikawa et al. (2016) study are D1UD01-8, -9 and -6. Their Lyα EWs estimated from spectroscopy are 7.8, 21.0, 81.5Å, respectively. The remaining two, Toshikawa source ID D1UD01-7 and D1UD01-10, do not meet our LAE selection because they are too faint in the $o3$ band (S/N in the range of 4–5); however, their $o3 - g$ colors, -1.61 ± 0.10 and -1.33 ± 0.08, are consistent with the

Lyα EWs, 36.2 and 34.3Å, measured from spectroscopy.

Sample Contamination At the central wavelength of the $o3$ filter (5024.9Å), the only plausible contaminants of our photometric LAE sample are [O II] emitters at $z \sim 0.35$, since our survey samples an inadequately small volume for [O III] emitters which would lie at $z \sim 0.01$. The adopted $o3 - g$ color cut corresponds to the observed line EW of 83Å, much larger than the values measured for [O II] emitters, which mostly range in $\lesssim 50$Å (Hogg et al. 1998; Ciardullo et al. 2013) at $z = 0.35$. The requirement that the galaxies have red $u - g$ colors provides an additional assurance that the Lyman break falls in the u band (i.e., the sources lie at $z > 2.7$).

Low-luminosity AGN with a broad Lyα emission line at $z > 2.7$ can potentially contaminate our LAE sample although the contamination is expected to be generally low (at $\sim 1\%$: Gawiser et al. 2006; Ouchi et al. 2008; Zheng et al. 2010; Sobral et al. 2018). We cross-correlate the source positions with the X-ray sources listed in the XMM survey in the field (Chiappetti et al. 2005), and find no match. However, the brightest source in our sample (QSO30046, $o3$=21.06, r=21.69 mag) is detected in the *Spitzer* MIPS 24 μm data. QSO30046 is also observed by the VIMOS VLT Deep Survey (VVDS: Le Fèvre et al. 2013) and classified as an AGN at $z_{\rm spec} = 3.86$. Given its redshift, the blue $o3 - g$ color is owing to broad emission from Lyβ and O VI (Vanden Berk et al. 2001). While we list its properties in Table 3, we remove this source from our LAE catalog.

We also cross-match our LAEs with spectroscopic redshift sources published by Toshikawa et al. (2016) and those in the VVDS and VIMOS Ultra Deep Survey (VUDS: Le Fèvre et al. 2015). Four matches are found; three are part of the LBG overdensity reported by Toshikawa et al. (2016) and the fourth lies at $z = 3.133$, but well outside it spatially. The relatively low number of matches is not surprising given that all these spectroscopic surveys are limited to sample only relatively bright sources (i.e., $i < 25$). In comparison, the mean i band magnitude of our LAE sample is ~ 26. Furthermore, the 'D1UD01' region is excluded from the VUDS survey coverage.

3.2. *Selection of LBG candidates*

We also identify a sample of UV-luminous star-forming galaxies at $z \sim 3$ by applying the Lyman break color selection technique to the ugr data from the CFHTLS T0007 catalog. The technique can identify star-forming galaxies with a modest amount of dust by detecting spectral features produced by the Lyman limit at $\lambda_{\rm rest} = 912$Å and absorption by the intervening Lyα forest at $\lambda_{\rm rest} = 912 - 1216$Å. At $2.7 < z < 3.4$, both of these features fall between the u and g bands.

In the right panel of Figure 3, we show the expected redshift evolution of broad-band colors from $z = 2.7$ in steps of $\Delta z = 0.1$. Four reddening parameters are assumed, E($B - V$)=0.0, 0.1, 0.2, and 0.3 (from left to right). The synthetic colors of lower-redshift galaxies are also computed using the Coleman et al. (1980) template of S0 galaxies redshifted out to $z = 2$ (black lines). As can be seen in the figure, most of the $z \sim 3.1$ sources are located at $u - g > 1.0$ while safely avoiding the locus of

$z < 2$ galaxies. Based on these considerations, we adopt the following criteria to select LBG candidates:

$$u - g > 1.0 \;\; \wedge \;\; -1.0 < (g - r) < 1.2$$
$$\wedge \;\; (u - g) > 1.5(g - r) + 0.75 \tag{2}$$

These are identical to those used by Toshikawa et al. (2016).

In the left panel of Figure 3, we show the locations of all the sources in the two-color diagram. For the sources undetected in the u band, we show lower limits by adopting the 2σ limiting magnitude (28.5 mag). We also require that the candidates be detected with more than 3σ (7σ) significance in the g (r) bands to ensure that their detection and color measurements are robust. A total of 6,913 galaxies are selected as our LBG candidates. 80 (86%) of the LAEs satisfy the adopted LBG criteria, with most of the remaining LAEs lying close to the selection criteria, confirming the similarity of the two populations. Our LBG catalog recovers 24 LBGs spectroscopically confirmed by Toshikawa et al. (2016) including all five 'D1UD01' sources. Of 6,913 galaxies, 210 have spectroscopic redshifts measured from the VVDS and VUDS surveys and by Toshikawa et al. (2016). Of those, 27 lie at $z < 2.7$ yielding a contamination rate of 13%.

The majority of these 27 galaxies have redshifts close to $z = 2.7$, suggesting that they are simply scattered into the LBG window. To quantify the role of photometric scatter, we carry out realistic galaxy simulations similar to those described in Lee et al. (2012). First, we create SEDs spanning a wide range of physical parameters (age, reddening, and redshift) and compute input photometry of these SEDs in the observed passbands. Mock galaxies are inserted into the images, and detection and photometric measurements are performed using the identical manner as the real data. The galaxies which satisfy our LBG criteria are collated into the master list. The redshift distribution of LBG-selected mock galaxies in the magnitude range $r = 22 - 28$ (matching the optical brightness of our LBG sample) peaks at $z \sim 3.1$ with a FWHM of ~ 0.7. Of those, 12% lie at $z < 2.7$, nearly identical to the contamination rate of 13% estimated from spectroscopy.

We make a qualitative comparison of the T0007 catalog with the Toshikawa et al. (2016, T16, hereafter) catalog. The major difference is a detection image which is a *gri*-based χ^2 image for the T0007 catalog and the *i*-band for the T16 catalog. The detection setting (including the threshold) is also different. Overall, we find that the T16 catalog is more inclusive of fainter objects with the median r-band magnitude of 26.5 mag, compared to 26.0 mag for the T0007 catalog. The two catalogs have 4,219 sources in common, which accounts for 61% and 54% of the T0007 and T16 catalogs, respectively.

3.3. *Search of Lyα Blobs*

We search for sources that are significantly extended in their Lyα emission; such sources are often referred to as a giant Lyα nebula or 'Lyα blob' (LAB, hereafter). The largest LABs reported to date can be as large as $\gtrsim 100$ kpc across (e.g., Dey et al. 2005). Multiple discoveries of luminous LABs in and around galaxy overdensities (e.g., Steidel et al. 2000; Matsuda et al. 2004; Palunas et al. 2004; Dey et al. 2005; Prescott et al. 2008;
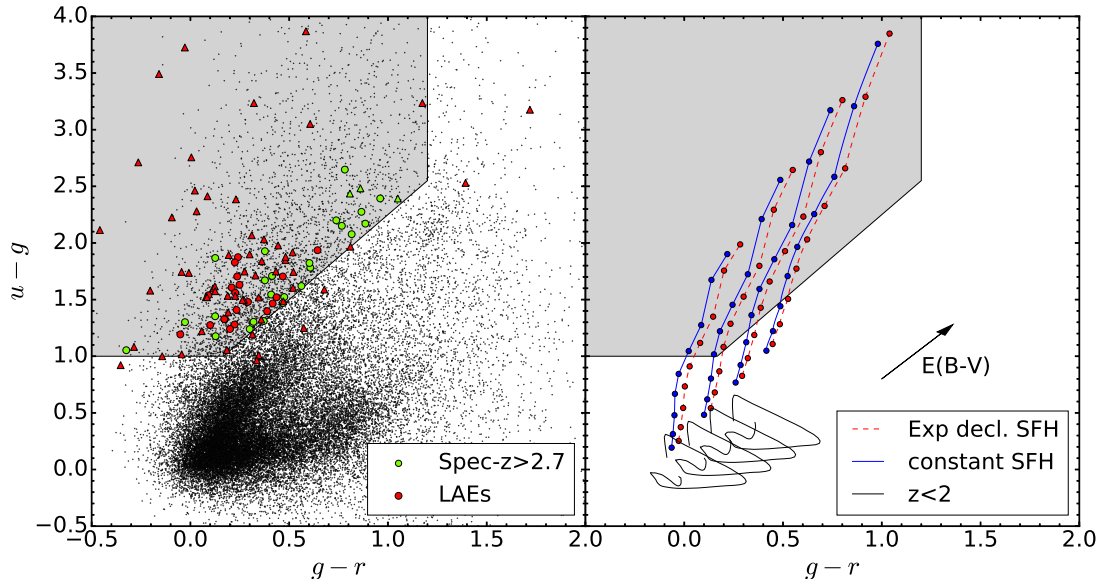
FIG. 3.— *Left:* $u - g$ vs $g - r$ colors of all r-band detected sources are shown in dots together with the LBG selection indicated by a grey shaded region. Red symbols are photometric LAEs while green symbols are known spectroscopic sources at $z_{spec} \geq 2.7$. All sources that are not detected in the u-band are shown as triangles using the 2σ limiting magnitude. *Right:* the redshift evolution of colors are illustrated for galaxies with dust reddening values. E$(B - V)$=0, 0.1, 0.2, 0.3 (from left to right). Galaxy's star formation rate is modeled to be constant (blue) or declining exponentially with time (red) as $\psi \propto \exp -(t/100 \text{ Myr})$. Along a given track, source redshift increases from $z = 2.7$ upwards with the interval $\Delta z = 0.1$. Black lines show expected colors of local spiral galaxies when redshifted out to $z = 2$.
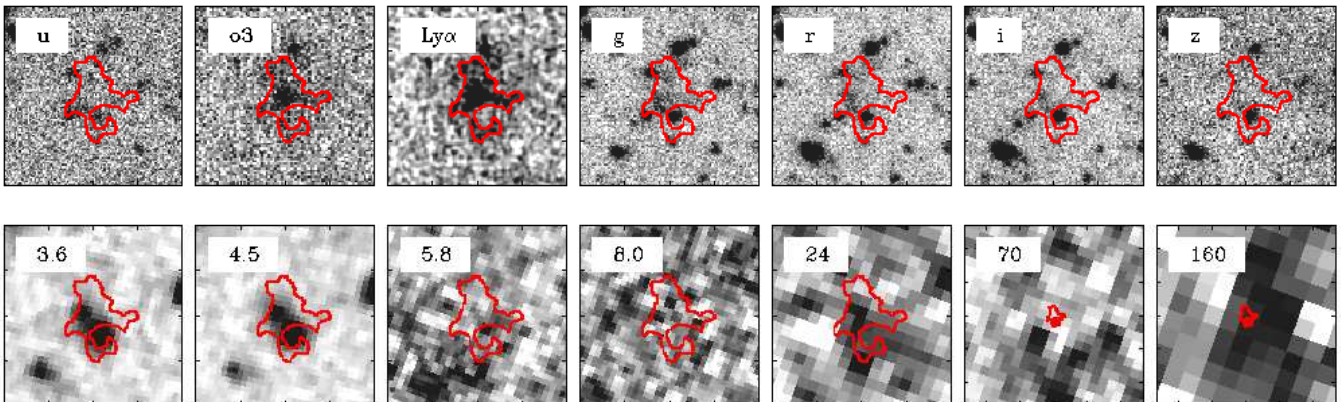

FIG. 4.— Postage-stamp images of the LAB candidate LAB17139. In all panels, north is up and east is to the left. Each image is $20''$ on a side except for the 70 μm and 160 μm data which are $80''$ on a side. A red contour outlines the boundary of the Lyα isophote (see text).

Yang et al. 2010; Mawatari et al. 2012; Bădescu et al. 2017) have led to a claim that they may be a signpost for massive large-scale structures.

To enable a sensitive search, we first create a Lyα line image by estimating and subtracting out the continuum emission from the $o3$ image. Following the procedure described in Xue et al. (2017, see their Eq. 11), the line flux is expressed as $F_{Ly\alpha} = af_{AB,o3} - bf_{AB,g}$, where f is the monochromatic flux density in the respective bands, and a and b are coefficients that depend on the corresponding bandwidth and optical depth of the intergalactic medium as well as the UV continuum slope. For example, at $z = 3.1$, with a UV slope β of -2.0, $a \sim 7.3 \times 10^{12}$ and $b \sim 7.7 \times 10^{12}$.

We run the SExtractor software (Bertin & Arnouts 1996) on the Lyα image as a detection band and per-

form photometry on the $o3$ and g band data. For detection, we require a minimum area of 16 pixels above the threshold 1.5σ which corresponds to 27.81 mag arcsec^{-2} or 1.80×10^{-18} ergs s^{-1} cm^{-2} arcsec^{-2}. Our LAB search is slightly different from our LAE selection in that source detection is made on the Lyα image, and is tuned to be more sensitive to extended low surface-brightness sources. The same $o3 - g$ color cut (Equation 1) as our LAE selection is applied. Our search yields a single Lyα blob candidate in the entire field, which we name LAB17139. It is also identified as an LAE. At the Lyα luminosity of $\approx 10^{43.3}$ erg s^{-1}, it has the highest luminosity in our LAE sample. We estimate the isophotal area to be 31.2 arcsec^2 (1,920 kpc^2 assuming $z = 3.13$). The postage-stamp images of LAB17139 are shown in Figure 4, and its properties are listed in Table 3.
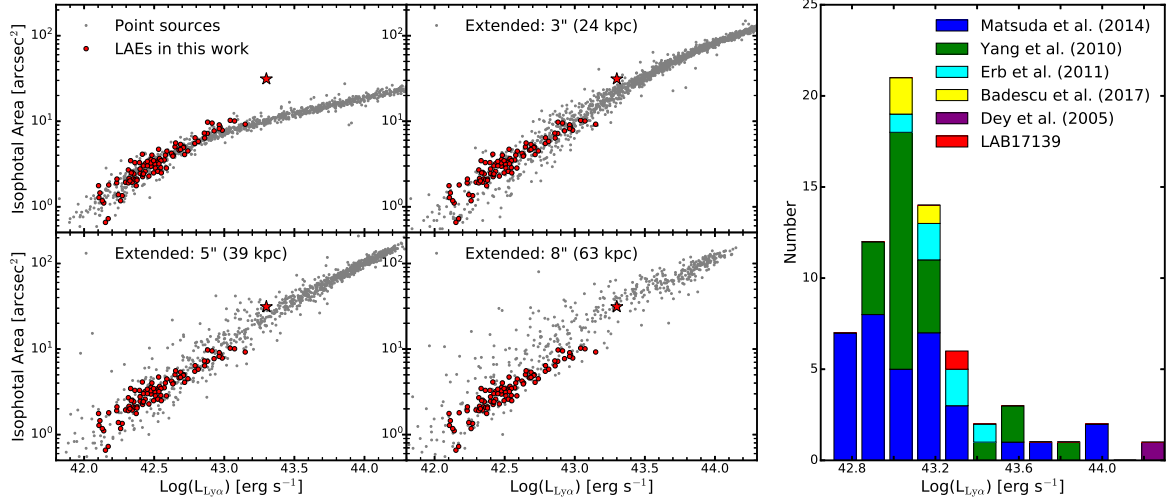
FIG. 5.— *Left:* the relationship between Isophotal size and intrinsic Lyα luminosity are determined through image simulations assuming that the intrinsic light profile is point-like or falls off exponentially with a half-light radius of 3″, 5″, and 8″. Grey points show simulated galaxies while red circles indicate the measurements from the LAEs in this study. The Lyα nebula, LAB17139, is marked as a red star in each panel. Given its observed luminosity and isophotal size, the half-light radius of LAB17139 is ∼ 40 − 55 kpc (see text). *Right:* the distribution of Lyα luminosities of known giant Lyα nebulae at $z = 2 - 4$ in the literature. LAB17139 is once again marked in red.

At the centroid of its Lyα emission, no apparent counterpart exists in any of the broad band data (gri). If its Lyα emission originates from a single galaxy, its continuum luminosity is fainter than $r=28.6$ mag (2σ). We do not find any plausible galaxy candidate in its vicinity that may lie at the same redshift. There are two UV bright sources just outside the isophote (one directly north and the other at the southwestern end); having the $u - g$ color of 0.57±0.19 and 0.90±0.12, neither of them satisfies our LBG selection. Therefore, it is unlikely they lie at the same redshift as LAB17139.

We search for its possible infrared counterpart utilizing two publicly available *Spitzer* observations in the D1 field, namely the *Spitzer* Wide-area InfraRed Extragalactic survey (SWIRE: Lonsdale et al. 2003) and the *Spitzer* Extragalactic Representative Volume Survey (SERVS: Mauduit et al. 2012). The former includes all IRAC and MIPS bands while the latter was taken as part of post-cryogenic IRAC observations (3.6 and 4.5μm bands only, which are deeper than the SWIRE counterpart). In Figure 4, we show postage stamp images of these data centered on LAB17139.

A single IR-bright source is identified within the LAB isophote which lies ≈1.2″ away from the center of LAB17139; the source is securely detected in the 3.6 and 4.5μm bands and marginally detected in the MIPS 24μm, but not in the 70μm band. In the optical (gri) images, the source appears very diffuse and spans at least 2″. If it is a single source, it is likely an interloper as it is too large to lie at $z \gtrsim 3$. Given its clear positional offset from the centroid of the LAB, it is unlikely that the source is solely responsible for the Lyα emission. Thus, the physical association of this diffuse source and LAB17139 remains unclear.

Intrinsic Size of LAB17139   We investigate the intrinsic size of LAB17139 by carrying out extensive image simulations. First, we insert artificial point sources with

a range of luminosities into the Lyα image after convolving them with the image PSF, and recover them using the same detection setting as our LAB search. On the top left panel of Figure 5, we show how measured isophotal size correlates with luminosity for point sources (grey symbols). It is evident that the majority of our LAEs follow the same sequence except for a few highest luminosity LAEs. On the other hand, LAB17139 lies well above the point-source locus: i.e., its high luminosity is insufficient to explain its large size.

Having established that the source is extended, we repeat the simulation but this time assuming that the radial profile of the source declines exponentially: $S(r) \propto \exp\left[-1.6783(r/r_s)\right]$. In Figure 5, we show the luminosity-isophotal area scaling relation for the sources with half-light radii of 3″ ($r_s = 1.8″$), 5″ ($r_s = 3.0″$), and 8″ ($r_s = 4.8″$); at $z = 3.13$, these values correspond to 24, 39, and 63 kpc, respectively. At a fixed line luminosity, the scatter in the recovered isophotal area increases with sizes as expected due to lower surface brightness. Nevertheless, Figure 5 shows that a unique scaling relation exists at a fixed intrinsic size.

Utilizing this trend, with luminosities fixed in the simulation, we estimate that the half-light radius of LAB17139 must lie in the range of 39–55 kpc, provided that its surface brightness falls exponentially. Based on the average stack of 11 Lyα blobs at $z = 2.65$, Steidel et al. (2011) reported the exponential scalelength of $r_s=27.6$ kpc, which corresponds to a half-light radius of 46.4 kpc. Thus, we conclude that LAB17139 has a similar size to $z \sim 2.6$ LABs.

In Figure 5 (right), we also show the line luminosity distribution of known Lyα blobs at $z=2–4$ (Matsuda et al. 2004; Dey et al. 2005; Yang et al. 2010; Erb et al. 2011; Bădescu et al. 2017). LAB17139 lies at a relatively high luminosity regime. The size distribution of LABs is more difficult to characterize because measured isophotal size of an LAB is determined by the

combination of intrinsic source brightness, redshift, and imaging sensitivity. For example, given everything equal, the same source can have larger isophotal size as the imaging depth increases. In order to construct the intrinsic size distribution of Lyα nebulae, image simulations such as the one adopted here are needed to be run on each of the relevant dataset.

4. SKY DISTRIBUTION OF GALAXIES

4.1. *A significant overdensity of LAEs at $z = 3.13$*

The LAE distribution in the sky appears to be highly inhomogeneous, suggesting that there may be overdense structures. To quantify their spatial distribution, we start by estimating the mean LAE density. After removing the regions near saturated stars (hatched circular regions in Figure 6), the effective area is 1,156 arcmin^2 over which 93 LAEs are distributed. Thus, the LAE surface density is $\bar{\Sigma}$=0.08±0.01 arcmin^{-2} where the error reflects the Poisson noise.

To create a LAE density map, we place point sources in the masked regions whose numbers are commensurate with that expected at random locations to avoid producing artificial under-densities. On the positional map containing 93 LAEs and point sources, we apply a Gaussian kernel of a FWHM of 10 Mpc (5.1′: $\sigma = 4.25$ Mpc). A similar smoothing scale has been used to identify LAE overdensities in the literature (e.g., Lee et al. 2014; Bǎdescu et al. 2017). The resultant map is shown in the top left panel of Figure 6 as contour lines and grey shades. The contour line values represent the local surface density relative to the mean value. The positions of individual LAEs are also shown.

The highest LAE overdensity is located ∼5′ west of the field center. Twenty one galaxies are enclosed within the purple contour (2.4$\bar{\Sigma}$ iso-density line), within which the effective area is 72.8 arcmin^2 (275 Mpc^2). We choose this region as the LAE overdensity. Scaling from the mean LAE surface density (0.08 arcmin^2), the expected number of galaxies within this region is 5.8 ± 2.4. Thus, the region contains 3.6 times more galaxies than expected ($\delta_\Sigma \equiv (\Sigma - \bar{\Sigma})/\bar{\Sigma} = 2.6 \pm 0.8$).

We recompute the mean density after excluding those in the LAE overdensity, and obtain $\bar{\Sigma}$=0.067 ± 0.008 arcmin^{-2}; this estimate is insensitive to inclusion or exclusion of the 'D1UD01' region which contains only a few LAEs. The revised overdensity is $\delta_\Sigma = 3.28 \pm 0.94$. Interestingly, LAB17139 is located at the outskirts of the LAE overdensity (see § 5.2 for more discussion).

We test the robustness of our overdensity estimate by computing the number of LAEs expected in our survey assuming the field Lyα luminosity functions at $z \sim 3.1$ (Gronwall et al. 2007; Ouchi et al. 2008). The expected number of LAEs in a magnitude bin $[m_k, m_k + \Delta m]$ and redshift bin $[z_j, z_j + \Delta z]$ is:

$$N_{\mathrm{LAE}}(z_j, m_k) = V_j p(m_k) S(z_j) \int_{L_k} \phi(L) dL, \quad (3)$$

where $S(z)$ is the normalized redshift selection function, defined from the effective filter transmission $T(\lambda)$ of the $o3$ filter expressed as $S(z_j) \equiv T(1215.67 \times (1 + z_j))/\max(T)$, V_j is the effective comoving volume, $p(m_k)$ is the completeness limit of the $o3$ image in the magnitude bin, which is derived from our image simulations of

point sources. For our calculation, we use $\Delta z = 0.003$ and $\Delta m = 0.1$ mag. The total number of LAEs is $N_{\mathrm{LAE}} = \sum_j \sum_k N_{\mathrm{LAE}}(z_j, m_k)$.

The expected number of LAEs in our field is 71±8 using the Gronwall et al. (2007) best-fit parameters and 102±10 using the Ouchi et al. (2008) values. As for the errors, we assume Poisson statistics, which are underestimated as they do not include cosmic variance. The observed number of LAEs in our survey field is consistent with that expected in an average field. Using these values as the field LAE density, the overdensity outlined by the purple contour in Fig 6 is $\delta_\Sigma = 2.2 - 3.6$, consistent with our previous estimate.

The significance of the newly discovered LAE overdensity is comparable to those found in known structures in the literature. Kurk et al. (2000a) reported an LAE overdensity of $\delta_\Sigma = 3$ around a radio galaxy at $z = 2.16$ (Venemans et al. 2007). Another radio galaxy at $z = 4.1$ is associated with an LAE overdensity of $\delta_\Sigma = 3.7$ (Venemans et al. 2002, 2007). The line-of-sight distances probed by these surveys are similar to this study ($\Delta z \approx 0.04 - 0.05$). Lee et al. (2014) reported two structures with similar LAE overdensities, which were later confirmed spectroscopically as protoclusters (Dey et al. 2016a).

4.2. *LAE vs LBG distributions*

If the LAE overdensity we discovered at $z \sim 3.13$ represents a genuine protocluster, the same region is expected to be traced by non-LAEs at the same redshift. Existing observations suggest that LAEs represent a subset of star-forming galaxies likely observed through sightlines with the lowest optical depths (Shapley et al. 2003) and otherwise obey similar scaling relations as UV color-selected star-forming galaxies (e.g., Lee et al. 2014; Shi et al. 2019). However, some LAEs appear to have lower metallicities, higher ionization parameters (Finkelstein et al. 2011; Nakajima et al. 2013; Song et al. 2014), and less massive with younger ages (e.g., Gawiser et al. 2007; Guaita et al. 2011; Hathi et al. 2016) than non-LAEs.

Isolating non-LAEs at the same redshift is a formidable task. In principle, similar to the LAE selection, one can look for narrow-band 'deficit' sources to find galaxies with strong Lyα absorption (e.g. Steidel et al. 2000). However, the depth of our imaging data is inadequate for this method to be effective. Alternatively, one can use the surface density of LBGs as a proxy to search for high overdensity regions. Using the Millennium simulations, Chiang et al. (2013) demonstrated that the progenitors of the most massive galaxy clusters reside in regions of elevated densities even at the redshift smoothing scale of $\Delta z \lesssim 0.2 - 0.3$. Observationally, several confirmed protoclusters are discovered initially as LBG overdense regions (e.g., Lee et al. 2014; Toshikawa et al. 2016).

To investigate the possibility of LBG overdensities, we use two LBG samples, namely, our fiducial LBG sample selected from the T0007 catalog, and the T16 catalog constructed by Toshikawa et al. (2016). The number of LBGs in these catalogs are slightly different: 6,913 and 7,793, respectively, which mainly reflects the differences in their source detection setting as discussed in Section 3.2.
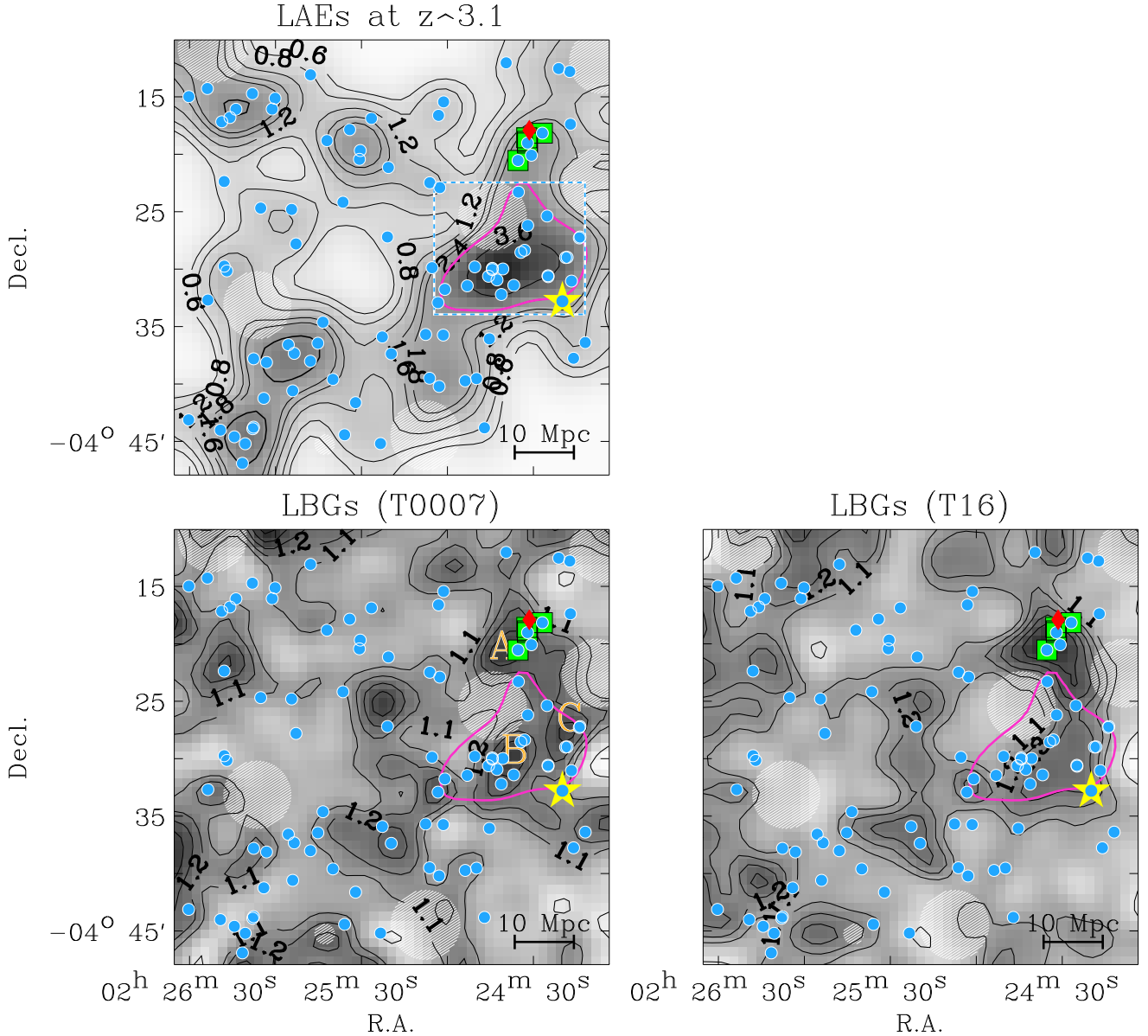
FIG. 6.— *Top left:* a smoothed density map of z=3.13 LAEs. Cyan circles show the LAE candidates while green squares indicate the five spectroscopically confirmed LBGs. The contours are constructed by smoothing the positions of the LAE candidates with a Gaussian kernel of FWHM=10 Mpc, and the contour labels show surface density levels relative to the field. The thick solid pink line outlines the LAEs overdensity region. Pixels near bright saturated stars are masked out (hatched circular regions), and do not contribute to the overdensity estimate (see text). The rectangle box is the region where we run K-S test for the LAEs and LBGs distributions. A large Lyα nebula (LAB17139: yellow star) and the brightest K_S band source (red diamond) are also shown. *Bottom left and Right:* similarly constructed density maps using LBGs selected from the official CFHTLS catalog (left) and the Toshikawa et al. (2016) catalog (right), respectively. For smoothing, a Gaussian kernel of FWHM=6 Mpc is used (see text for discussion). Three LBG overdensities are labelled as 'A', 'B', and 'C'. Positions of individual LBGs are not shown for clarity; other symbols are identical to those in the left panel.

Similar to the LAE density map, we smooth the positions of each LBG using a Gaussian kernel. In determining the size of a smoothing kernel, two factors need to be taken into consideration: the source surface density and the volume within which a galaxy overdensity is enclosed. For instance, using a kernel size smaller than the typical distance between two nearest neighbors is undesired as most 'overdensities' will consist of a single galaxy. On the other hand, using too large a kernel size effectively averages out cosmic volumes that are much greater than a typical size of a galaxy overdensity, thereby washing away the very signal one is searching for.

In the case of LBGs, the source density is sufficiently high (and the distance to the nearest neighbor small) that the cosmic volume consideration becomes the main determinant of the kernel size. Toshikawa et al. (2016) used a tophat filter with a diameter 1.5 Mpc (physical) in their search of $z \sim 3-6$ LBG overdensities. The size was justified as a typical angular size enclosing protoclusters in cosmological simulations (Chiang et al. 2013). At $z = 3.13$, this corresponds to 6.2 Mpc.

In the bottom left and right panels of Figure 6, we

show the resultant LBG maps using a smoothing FWHM of 6 Mpc. Grey scales and contour lines indicate the density fluctuations together with the positions of the LAEs (cyan circles), and five spectroscopic sources at $z = 3.13$ (green squares).

Several overdensities are present but each with a much lower significance than our LAE overdensity. This is not surprising considering the line of sight distances sampled by them. Our image simulation suggests that the FWHM in the redshift selection function, at $r \approx 24.5$, is $\Delta z = 0.7$ corresponding to 666 Mpc. Using the $o3$ filter FWHM, the LAE redshift range is $z=3.109$–3.155, spanning just 44 Mpc in the line-of-sight distance, more than an order of magnitude smaller than that of the LBGs. The large Δz of the LBGs can also result in artificial overdensities because of chance alignments along the line of sight. It is easy to understand that, even in a sightline of a massive protocluster, LBGs with no physical association with the structure will outnumber those in it.

In both LBG density maps (T0007 and T16 LBG samples), smaller overdensities as well as underdense regions spanning $\gtrsim 20$ Mpc are found in identical locations, and the largest and most significant overdensity structures are found at the western end of the field. In the T0007 map, the region consists of three adjacent overdensities labelled as 'A', 'B', and 'C' in Figure 6. In the T16 map, the overdensity A is noticeably more pronounced while the B and C overdensities, which are merged into a single overdensity, appear less significant.

The LAE overdensity largely coincides with the 'B+C' region, and stretches toward the 'A' region where a concentration of four LAEs lies. It is intriguing that in the 'A' region, which Toshikawa et al. (2016) found to be the most significant LBG overdensity, relatively few LAEs are found. Assuming that all LAE candidates lie at $z = 3.13$, there are a total of just six galaxies in the 'A' region (including the spectroscopic sources that barely escape the LAE selection). In comparison, the LAE overdensity contains 21 LAEs. Extending the overdensity region slightly would include additional two LAEs and one Lyα nebula (Section 3.3).

Comparing the LAE and LBG maps, it is evident that their sky distributions are disparate. Other than the main LAE overdensity, none of the LAE density peaks coincides with the LBG overdensities. This likely suggests that there is only a single large-scale structure that exists at $z = 3.13$, and smaller LAE overdensities are a product of Poisson fluctuations, or alternatively, belong to much less significant cosmic structures than the one which the main LAE overdensity inhabits.

Next, we make a quantitative comparison of the LBG and LAE distributions in the general LAE overdensity region. To this end, we perform a series of two-dimensional Kolmogorov-Smirnov tests (Peacock 1983; Fasano & Franceschini 1987). We define a rectangular region enclosing the LAE overdensity as outlined in the left panel of Figure 6 whose area is 115 arcmin^2. Running the 2D K-S test in the LBG and LAE distributions yields the p value of 0.28 (0.20) using the fiducial (T16) LBG samples. The large p value indicates the similarity of the two distributions.

As the 2D K-S test is less reliable than the one-dimensional test, we perform a control test to interpret the p values. First, we create two random samples that are uniformly distributed in the rectangular region, each matching the number of LAEs and LBGs in our samples, and calculate the corresponding p value. The process is repeated 1,000 times and the p value is recorded each time. We obtain a median (mean) p value of 0.23 (0.27). Second, we assume that the underlying distribution is a two-dimensional Gaussian function with $\sigma=5'$ centered at the middle of the rectangle, and repeat the test, obtaining similarly large p values (median and mean value of 0.27 and 0.31).

Finally, we test the similarity of the two galaxy samples in the entire field by moving the rectangle to random locations. Whenever a masked region falls within the subfield, we randomly populate the area with the expected number of point sources therein before performing the test. The median (mean) p-value is 4.5×10^{-15} (9×10^{-4}). These tests give strong support to the possibility that the cosmic structure traced by the LAE overdensity is also well populated by LBGs at a level not observed in other parts of the survey field.

All in all, our analyses strongly suggest a presence of a significantly overdense cosmic structure, which includes 21 LAEs, 5 spectroscopically confirmed $z = 3.13$ LBGs, and one luminous Lyα nebula. A large number of LBGs exist in the general region although, without spectroscopy, it is difficult to know how many of them truly belong to the structure. A segregation of the highest LAE and LBG overdensity is also curious. We discuss possible implications of our results in Section 5.2.

5. DISCUSSION

5.1. Descendant mass of the protocluster

5.1.1. The present-day mass of the LAE overdensity

Given that the $o3$ filter samples $\approx$44 Mpc in the line-of-sight direction, a surface overdensity computed based on the angular distribution of galaxies should scale closely with a given intrinsic galaxy overdensity with a minimal contamination from fore- and background interlopers. In this section, we estimate the true galaxy overdensities, and infer their descendant (present-day) masses.

Based on the Millennium Runs (Springel et al. 2005), Chiang et al. (2013) calibrated the relationship between galaxy overdensity (δ_g) and present-day mass $M_{z=0}$ at a given redshift. Galaxy overdensity is measured in a $(15 \text{ Mpc})^3$ volume ($\delta_{g,15}$ hereafter) using the galaxies whose host halos have the bias value of $b \approx 2$. This value is comparable to that typically measured for LAEs (Gawiser et al. 2007; Guaita et al. 2010; Lee et al. 2014), which lie at similar redshift and are of comparable line luminosities to those in our sample. Thus, it is safe for us to apply the Chiang et al. calibration without further corrections.

The transverse area enclosing the LAE overdensity is 275 Mpc^2, reasonably close to that of $(15 \text{ Mpc})^2$ used by Chiang et al. (2013). However, the line-of-sight distance sampled by the $o3$ filter is $\sim$3 times larger than their sampled volume. Generally, averaging over a larger volume reduces the significance of the overdensity. We correct this effect using their Figure 13 where they show how, for a fixed $\delta_{g,15}$, measured (surface) overdensity drops with increasing redshift uncertainty Δz. Correcting the measured overdensity (§ 4.1) accordingly results in $\delta_{g,15} = 5.5 \pm 1.6$. Inferred from Figure 10 of

Chiang et al. (2013), the corresponding descendant mass at $z = 0$ is $M_{\rm tot} \approx (0.6 - 1.3) \times 10^{15} M_\odot$. The estimated overdensity well exceeds the value $\delta_{g,15} = 3.14$, above which there is $>80\%$ confidence that it will evolve into a galaxy cluster by $z = 0$. These considerations lend confidence that the newly identified LAE overdensity is a genuine massive protocluster.

Alternatively, a more empirical method may be employed similar to that taken by Steidel et al. (1998). If all mass enclosed within the overdensity will be gravitationally bound and virialized by $z = 0$, the total mass can be expressed as:

$$M_{z=0} = (1 + \delta_m)\langle \rho \rangle V_{\rm true} \qquad (4)$$

where $\langle \rho \rangle$ is the mean density of the universe, and $V_{\rm true}$ is the true volume of the overdensity. The matter overdensity δ_m is related to the galaxy overdensity through a bias parameter. The bias parameter b can be described as $1 + b\delta_m = C(1 + \delta_g)$ where C represents the correction factor for the effect of redshift-space distortion due to peculiar velocities. The true volume $V_{\rm true}$ is underestimated by the same factor as $V_{\rm true} = V_{\rm obs}/C$. In the simplest case of spherical collapse, it is expressed as:

$$C(\delta_m, z) = 1 + \Omega_m^{4/7}(z)[1 - (1 + \delta_m)^{1/3}]. \qquad (5)$$

Equation 5 and the equation relating the matter and galaxy overdensity can be evaluated iteratively to determine C and δ_m. The observed overdensity is $\delta_g = 3.3 \pm 0.9$ and the estimated survey volume of $V_{\rm obs} = 1.21 \times 10^4$ Mpc^3. The bias value is assumed to be $b \approx 2$ (Gawiser et al. 2007; Guaita et al. 2010; Lee et al. 2014). We obtain the matter overdensity in the range of $\delta_m = 0.8 - 1.3$; thus the total mass enclosed in this overdensity is $M_{z=0} \approx (1.0 - 1.5) \times 10^{15} M_\odot$, in good agreement with the simulation-based estimate. We conclude the LAE overdensity will evolve into a Coma-like cluster by the present-day epoch (see, e.g., Kubo et al. 2007).

5.1.2. *The structure and descendant mass of the LBG overdensity*

As discussed in Section 4.2, there appear to be multiple LBG overdensities; these regions are marked as 'A', 'B', and 'C' in Figure 6. The 'B' and 'C' overdensities are merged into one in the T16 catalog, and lie in a region largely overlapping with the LAE overdensity, hinting at their physical association. On the other hand, the 'A' overdensity – ≈ 15 Mpc away from the LAE overdensity – may be a separate system and is largely devoid of LAEs therein. As such, we consider the 'B+C' and 'A' as two separate structures and evaluate their significance.

The LBG color criteria (§ 3.2) typically result in a relatively wide redshift selection, $\Delta z = 0.4 - 0.6$. The redshift range of spectroscopic sources yields the median redshift of $z = 3.2$ with the standard deviation 0.6, in a reasonable agreement with the FWHM Δz estimated from our photometric simulations (Section 4.2). This very wide Δz makes it challenging to directly use the Chiang et al. (2013) calibration. Instead, we use an alternative method described in Shi et al. (2019) to estimate the intrinsic galaxy overdensity as follows.

We create a mock field, which is of the same size as our survey field and contains a single protocluster with a galaxy overdensity δ_g. The protocluster overdensity is assumed to extend a transverse size of the LBG overdensity ('A') and 15 Mpc in the line-of-sight distance. We divide the redshift range $z = [2.7, 3.4]$ into 35 bins each with $\Delta z = 0.02$ ($\sim$19 Mpc). The number of galaxies belonging to the protocluster is then expressed as $N_{\rm proto} = (1 + \delta_g)N_{\rm all}/(35 + \delta_g)$ where $N_{\rm all}$ is the total number of LBGs in the field. We populate the remainder ($N_{\rm all} - N_{\rm proto}$) at random in the redshift and angular space. As for the protocluster galaxies, they are also randomly distributed but are confined within the overdense region. Based on the galaxy positions, we construct the surface density map in the identical manner to the real data, and estimate the mean overdensity within the protocluster region. We repeat the procedure 10,000 times while varying the intrinsic overdensity δ_g in the range of 1–30, and obtain a relationship between the observed surface density and the intrinsic overdensity.

For the level of observed overdensity for the 'A' and 'B+C' regions, we choose the $1.3\bar{\Sigma}$ iso-density contour based on our fiducial LBG catalog; the transverse area of these regions are 36 and 27 arcmin^2, respectively; the 'B' and 'C' contours are disjoint and we simply add the enclosed regions. Using our simulation as described above, the intrinsic overdensities of the 'A' and 'B+C' regions are δ_g of $(18.4 - 28.4)$ and $(14.4 - 23.0)$, respectively. We assume that their galaxy bias is $b_{\rm LBG} \approx 2.6$, i.e., slightly higher than that of the LAEs (Bielby et al. 2013; Cucciati et al. 2014). Using Equation 4 again, we obtain the total masses of these structures $(0.6 - 1.0) \times 10^{15} M_\odot$ and $(0.4 - 0.6) \times 10^{15} M_\odot$, respectively. Increasing the bias value to $b_g = 3$ would decrease the mass by 13%; decreasing it to a value similar to the LAE bias would have the opposite effect on the mass. Generally, our mass estimate is relatively insensitive to a specific choice of isodensity value. This is because lowering the density contrast tends to increase the effective area at a lower overall density enhancement, while raising it has the opposite effect.

We repeat our mass estimates using the T16 catalog which yields slightly different levels and angular extent of the overdensities. The resultant masses for the two structures are $(0.8 - 1.1) \times 10^{15} M_\odot$ and $(0.4 - 0.6) \times 10^{15} M_\odot$. The 'A' structure has $\approx 20\%$ larger mass, reflecting its more pronounced density contrast in the T16 catalog; the estimate for the 'B+C' region is consistent with the earlier estimate.

Having estimated the LBG-traced total (descendant) masses of both regions, it is worth contrasting them with the inferred values had we used the LAEs as tracers instead. In the 'A' region, only three LAEs exist resulting in an insignificant overdensity $\delta_g = 0.6 \pm 0.3$, and $M_{\rm tot} \sim (2 - 4) \times 10^{14} M_\odot$, much smaller than the LBG-inferred values. For this calculation, we assume the surface area (36 arcmin^2) defined by the LBG distribution, which is clearly much larger than the ill-defined area which the three LAEs populate. Thus, the resultant mass should be regarded as an upper limit. As for the 'B+C' region, the disagreement of the inferred masses is less severe: we prviously obtained $\sim (0.6-1.3) \times 10^{15} M_\odot$ and $(0.4 - 0.6) \times 10^{15} M_\odot$ for the LAE- and LBG-based estimates, respectively. If we were to use the surface area of the 'B+C' region defined by the LBGs, the for-

mer becomes $\sim (0.6 - 0.9) \times 10^{15} M_\odot$, further alleviating the tension. Nevertheless, it is obvious that these galaxy types do not yield consistent mass estimates. In Section 5.2, we discuss several physical scenarios which may be responsible for this disagreement.

5.2. *On the possible configuration of the structures and their constituents*

The observational data presented in this work paint an incomplete picture leaving several unanswered questions. First, the spatial segregation between the LAE- and LBG-traced structure is puzzling because the spectroscopically confirmed sources in the latter lie at the same redshift as the former. If the galaxies in the LBG overdensity trace a single structure, the implication would be that the structure 'A' genuinely lacks Lyα-emitting galaxies whereas the structure 'B+C' is populated by both LAEs and LBGs (and one large Lyα nebula).

The expected comoving size of galaxy clusters observed at $z \sim 3$ ranges in 15–20 Mpc (Chiang et al. 2013), in agreement with recent estimates of several confirmed protoclusters (Dey et al. 2016a; Bǎdescu et al. 2017). In comparison, the projected end-to-end size of the combined structure, at ≈ 30 Mpc, is simply too large, suggesting that the two are two separate structures. If they lie at the same redshift (i.e., the projected distance is close to the true separation), the dynamical timescale ($\tau \sim \sqrt{R^3/GM}$) is in the order the Hubble time.

If 'A' and 'B+C' represent two separate systems, we speculate several physical scenarios consistent with the current observational constraints. First, we may be witnessing galaxy assembly bias: a baryonic response to the well-known *halo assembly bias*. The latter generally refers to the fact that the spatial distribution of dark matter halos depends not only on mass but also on other properties such as concentration parameter, spin, large-scale environment, and halo formation time (e.g., Gao et al. 2005; Wechsler et al. 2006; Li et al. 2008; Zentner et al. 2014). In the present case, a given halo's environment and formation time are particularly relevant considering that clusters are expected to be the sites of the earliest star formation in the densest environment.

Zehavi et al. (2018) examined the importance of the halo formation time and its large-scale environment in determining the halo mass (M_h) to stellar mass (M_{star}) and the halo mass to the clustering strength scaling relations. They found that, while controlling for M_h, halos with an earlier formation time tend to host galaxies with larger M_{star}, have fewer satellites, and are more strongly clustered in space compared to those that formed at a later time. Similar dependence was found for the halos' large-scale environment (measured as dark matter density smoothed in a $5h^{-1}$ Mpc scale where $h = 0.7$) where a higher density and earlier formation time have similar effects on galaxies' properties.

In this context, we speculate that the 'B+C' structure may have formed more recently than the 'A', and thus is traced by numerous young and low-mass galaxies, many of which are observed as LAEs (see, e.g., Guaita et al. 2010, 2011). In comparison, as an older and more settled system, the 'A' protocluster has had more time to accrete surrounding matter and to merge with lower-mass satel-

lite halos, and thus is expected to have more evolved (i.e., more stars and dust) star-forming galaxies that are observed as LBGs, while having fewer low-mass systems such as LAEs. Zehavi et al. (2018) also found a strong variation in their clustering amplitude at scales 5–10 Mpc (see their Figure 10). One implication may be that it is not appropriate to use a galaxy bias representative of the field galaxy population of the same type (as we have done in Section 5.1) in estimating the total descendant mass of a structure that likely formed the earliest.

A slight variant of the above hypothesis is that, while the two have similar present-day masses, 'A' is simply a more massive and relaxed halo at the time of observation than 'B+C', which is an aggregate of two or more of smaller halos. Similar environment-dependent processes are expected to those in the assembly bias scenario.

In these conjectures, it follows that both LAE- or LBG-based protocluster searches would be sensitive to different evolutionary stages (or ages) of cluster formation in which the former (latter) method favors younger (older) structures. Similarly, the presence of galaxies with old stellar populations should be predominantly found in the LBG-selected structures but not in LAE-traced ones. While several known structures support this picture (Steidel et al. 2005; Wang et al. 2016; Shi et al. 2019), only a handful of protocluster systems have been characterized using multiple galaxy tracers (including LAEs: e.g., Steidel et al. 2000; Kurk et al. 2000b, 2004) in a similar manner to the present work, making it difficult to evaluate the validity of such a hypothesis. A rigorous test would require a well-controlled statistical approach in which large samples of LBG- and LAE-selected overdensities are identified independently and compared for the level of their cohabitation. The same test can also inform us about how baryonic physics can impact the manner in which galaxies trace the underlying large scale structure in dense environments (e.g., Orsi et al. 2016).

The final and most innocuous scenario to explain the curious configuration of 'A' and 'B+C' is as follows: the spectroscopically confirmed sources embedded in the 'A' region may be spatially disjoint from the majority of LBGs therein, and are part of a small group falling in towards the 'B+C' structure. The 'A' region then could represent just another protocluster with no physical association with the LAE overdensity. It is unlikely, however, because within the 'A' region Toshikawa et al. (2016) confirmed 30 galaxies between $z = 2.73$ and $z = 3.56$, and there was only one significant redshift overdensity at $z = 3.13$. More extensive spectroscopy in all of the 'A+B+C' regions can elucidate the true configurations of these structures.

Finally, we contemplate on the significance of the Lyα nebula in the context of protocluster formation. As described in § 3.3, our search of the entire field resulted in a single LAB. The fact that it is located at the southwestern end of the LAE overdensity ('B+C') is significant.

There is mounting evidence that luminous Lyα nebulae are preferentially found in dense environments. Matsuda et al. (2004) identified 35 Lyα nebulae candidates in an LAE and LBG rich protocluster at $z = 3.09$, and reported that the LAEs and LABs trace one another. Yang et al. (2010) conducted a systematic search

for LABs in four separate fields, each comparable in size to our survey field. The number of LAB they identified in each field ranged in 1–16; they argued that high cosmic variance implies a very large galaxy bias expected for group-sized halos. Small groups of galaxies are observed to be embedded in several luminous blobs (e.g., Dey et al. 2005; Prescott et al. 2012; Yang et al. 2011, 2014) in agreement with Yang et al. (2010)'s assessment.

It is notable that LAB17139 lies at the periphery of the 'B+C' overdensity traced by LAEs. Recently, Bădescu et al. (2017) compiled the LAE/LAB data for five protoclusters at $z = 2.3$ and $z = 3.1$, and showed that LABs are preferentially found in the outskirts of each of the LAE overdensities. They speculated that these blobs may be signposts for group-sized halos (harboring galaxy 'proto-groups') falling in towards the cluster-sized parent halo traced by LAEs where Lyα-lit gas traces the stripped gas from galaxy-galaxy interactions.

A significant variation of their numbers implies a relatively short timescale for the LAB phenomenon; that combined with their preferred locations at the outskirts requires a physical explanation involving the protocluster environment. The kinematics of protocluster galaxies showing relatively low velocity dispersions[11] and in multiple groupings ($\lesssim 400$ km s^{-1}: Dey et al. 2016a) indicate that the structure is far from virialization.

If a galaxy overdensity is a superposition of multiple overdensities in physical proximity, LAB's preferred location at their outskirts may signify their first group-group interactions enabling a host of galaxy-galaxy interactions which in turn bring about starbursts, AGN, and stripped gas lighting up an extended region surrounding these galaxies.

5.3. The physical properties of LAEs and their environmental dependence

We investigate whether local environment influences the properties of the LAEs. To this end, we define two LAE subsamples according to their measured galaxy surface density. The 'overdensity' sample includes 21 LAEs within the purple contour shown in Figure 6 as well as three of the Toshikawa et al. (2016) galaxies that we recover as LAEs. The remaining 69 LAEs belong to the 'field' sample.

Apart from the line luminosities and EWs (§ 2.2), we also convert the measured UV continuum slope, β, to the extinction parameter $E(B - V)$ assuming the dust reddening law of local starburst galaxies (Calzetti et al. 2000). For the sources with relatively robust β measurements ($\Delta\beta < 0.9$), we also derive dust-corrected SFRs by correcting the continuum luminosity accordingly using the Kennicutt (1998) calibration. In the overdensity and field sample, 21 (88%) and 42 (61%) LAEs have the SFR estimates. The difference stems from the fact that the former sample is on average more UV-luminous (see later). However, our SFR estimates are only approximate given a relatively large uncertainty in the measured

UV slopes; increasing (decreasing) β value by $\Delta\beta = 0.4$ (which is well within a typical uncertainty) would lead to a 41% increase (58% decrease) in the SFR estimate.

The mean properties of each subsample are listed in Table 2 with the errors corresponding to the standard deviation of the mean, and the overall distributions of these parameters are illustrated in Figure 7. In both, we show our results for the full sample containing 93 LAEs (top), and for the 63 LAEs with reliable SFR estimates (bottom). We find that our conclusions do not change depending on which sample we consider.

In terms of both line and continuum luminosities, we find a possible enhancement for the LAEs in the overdense regions compared to those in the field. The enhancement in UV luminosity is 74±32% if we compare all LAEs in both samples, and 58±22% if only the LAEs with robust β measurements are considered. As for Lyα line luminosity, the enhancement relative to the field is 32±15% and 55±18% for all LAEs and those with β measurements, respectively. The median EW and $E(B - V)$ values are comparable in both samples.

To assess the similarity of the overall distribution of the physical quantities between the two samples, we perform the one-dimensional K-S test. The p values obtained for each distribution are indicated in Figure 7. The values obtained for the Lyα and UV luminosity distributions lie around $p \sim 0.05$ corresponding to a 2σ in the confidence level. As for the EWs and UV slopes β, the distributions are statistically indistinguishable for the two environmental bins.

The same trend is visualized in Figure 8. In the left panel, we show the LAE positions overlaid with a two-dimensional Voronoi tessellated map of the whole field (Marinoni et al. 2002; Cooper et al. 2005). Each LAE is embedded in a Voronoi polygon with an area A_V, and its 2D density scales inversely with the radius of the equivalent circular region defined as $r_V \equiv \sqrt{A_V/\pi}$. The map is color-coded by the 2D density, with the size of each star increases with increasing density. The LAE overdensity clearly stands out as a region with the highest concentration of blue stars.

In the other two panels of Figure 8, we show the same tessellated LAE map but the LAEs are color-coded by Lyα (middle) and UV luminosity (right), respectively. A large fraction of blue stars representing a top third populate the combined region of the LBG and LAE overdensities. The trend is particularly evident for the case of continuum luminosity (right panel). Of the total 30 blue stars, 17 (57%) reside within the LAE overdensity region. No radial dependence is found for the luminosity enhancement within the group although our sample may be too small to discern any trend.

The overall correlation between the LAE density and its luminosity, and the level of enhancement are consistent with the similar trends we reported in Dey et al. (2016a) for the constituents of another protocluster at $z = 3.78$. The present work takes a step further by examining the UV and line luminosity of the same galaxies, which was not possible previously due to the relatively shallow depth of the broad-band data.

The higher UV- and Lyα mean luminosities observed for protocluster LAEs are curious and cannot be fully explained by the level of overdensity. If the protocluster

---

[11] Matsuda et al. (2005) reported a much larger velocity dispersion of $\sim$1100 km s^{-1} for the SSA22a protocluster at $z = 3.09$; however, the spectroscopic LAEs have at least three separate groups. We estimate that the velocity dispersion of each group does not exceed 500 km s-1 (see Dey et al. 2016a, for detail).

	N	$W_{0,\mathrm{Ly}\alpha}$ [Å]	$\log(L_{\mathrm{UV,obs}})$ [erg s^{-1} Hz^{-1}]	$\log(L_{\mathrm{Ly}\alpha,\mathrm{obs}})$ [erg s^{-1}]	$E(B-V)$	SFR$_{\mathrm{UV,cor}}$ [M$_\odot$yr^{-1}]
			All Galaxies			
Overdensity	24	75 (57) ± 16	28.05 (28.08) ± 0.08	42.57 (42.53) ± 0.05	-	-
Field	69	104 (53) ± 16	27.81 (27.84) ± 0.06	42.45 (42.38) ± 0.04	-	-
All	93	96 (55) ± 13	27.87 (27.93) ± 0.05	42.52 (42.42) ± 0.03	-	-
			Galaxies with β Measurements			
Overdensity	21	52 (49) ± 5	28.20 (28.24) ± 0.07	42.67 (42.65) ± 0.05	0.11 (0.06) ± 0.03	15 (6) ± 6
Field	42	62 (46) ± 9	28.00 (27.99) ± 0.06	42.48 (42.38) ± 0.05	0.13 (0.14) ± 0.02	10 (5) ± 2
All	63	59 (47) ± 6	28.06 (28.05) ± 0.05	42.52 (42.42) ± 0.04	0.13 (0.10) ± 0.02	11 (5) ± 2

Note. — The values represent means of key physical properties (medians in the brackets) with uncertainties for each sample.
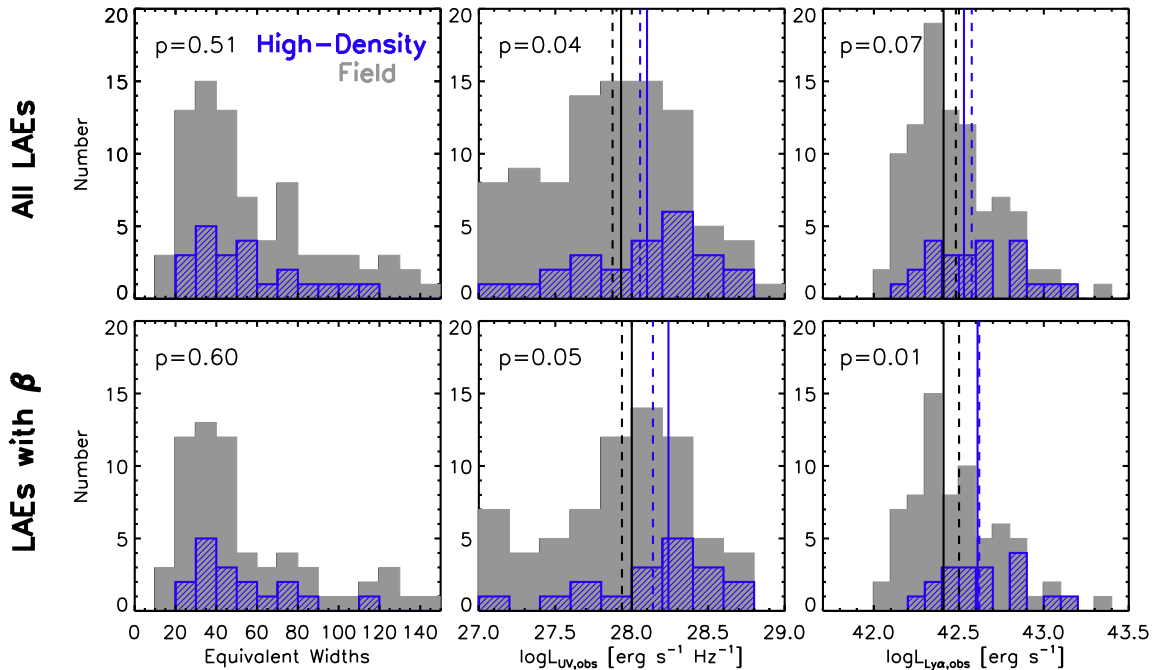

Fig. 7.— Histograms of rest-frame equivalent widths (left), observed UV luminosity (middle), and observed Lyα luminosity (right) of two subsamples. Blue hatched and grey histograms represent high-density LAEs and field LAEs, respectively. The median p values obtained from the Kolmogorov-Smirnov test are shown in each panel. The vertical solid lines are the mean values while the dashed lines are the median values.

LAEs obey the same UV or Lyα luminosity function as measured in the field but are simply scaled up by a factor of $(1+\delta_g)$, the expected mean or median values would be identical to those in the field. Observationally, the trend can be due to either the lack of low-luminosity (and low-mass) galaxies or the excess of high-luminosity LAEs in overdense environments relative to the field.

The lack of low-luminosity, low-mass galaxies near cluster-sized halos may be caused by a variety of astrophysical processes. Orsi et al. (2016) showed that AGN feedback (from a quasar or radio galaxy hosted by the central halo) can alter the clustering and abundance of galaxies inhabiting the satellite halos. They also noted that the spatial distribution of LAEs may be more affected than other galaxy tracers – such as Hα emitters – due to complex radiative transfer effects. Cooke et al. (2014) studied a radio galaxy MRC 2104-

242 at $z = 2.5$ and reported the lack of low-mass galaxies ($M_{\mathrm{star}} \lesssim 10^{10} M_\odot$) in their 7 arcmin^2 survey field. It is certainly conceivable that there was a radio galaxy or quasar in the past (which has since then turned off), which had influenced the formation histories of these galaxies. While these trends warrant further exploration with upcoming surveys such as DESI, it is far from conclusive at this time given the small sample size and areal coverage. Further, the most likely candidate hosting a powerful AGN is not at the center but at the outskirts of this structure. Future availability of deep near-infrared imaging would be helpful in closer examination of the stellar mass distribution and its radial dependence, which can be compared with those in galaxy simulations.

Alternatively, our results can be interpreted as a mild but widespread enhancement of star formation in the protocluster LAEs. One possible explanation for the
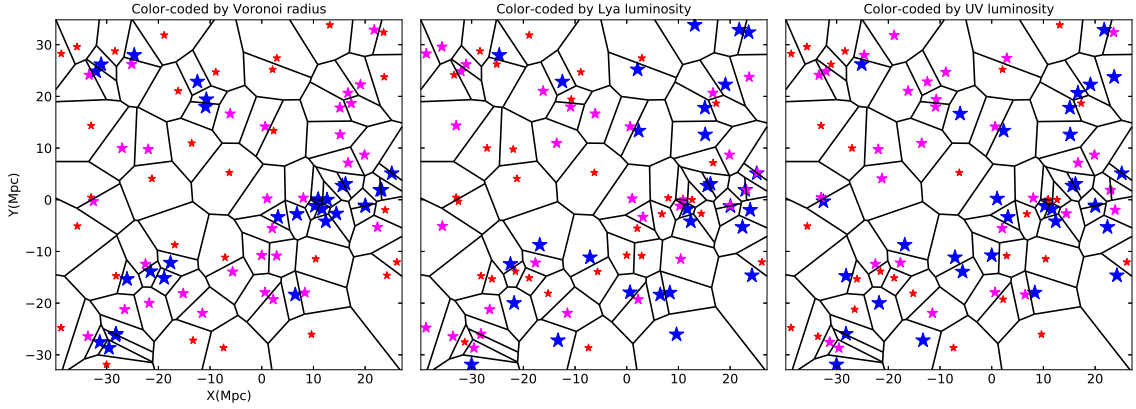
FIG. 8.— Voronoi tessellated maps of the LAE positions. The LAE sample is divided by Voronoi radius (left), Lyα luminosity (middle), and UV luminosity (right) of each LAE. In all panels, blue, pink and red colors are used for the top, middle, and bottom third, corresponding to $r_V \leq 3.2$, $3.2 < r_V \leq 4.85$, and $r_V > 4.85$ in Voronoi radius, $\log(L_{\mathrm{Ly}\alpha}) > 42.60$, $42.38 < \log(L_{\mathrm{Ly}\alpha}) \leq 42.60$, and $\log(L_{\mathrm{Ly}\alpha}) \leq 42.38$ in line luminosity, and $\log(L_{\mathrm{UV}}) > 28.06$, $27.68 < \log(L_{\mathrm{UV}}) \leq 28.06$, and $\log(L_{\mathrm{UV}}) \leq 27.68$ in UV luminosity. The correlation between these parameters is evident as a large fraction of UV-/Lyα-luminous galaxies are found in the LAE overdensity region.

higher luminosity value may be that the luminosity function (and SFR function) is more 'top-heavy' in protocluster environment, producing a larger fraction of UV-luminous galaxies. This may be brought on by faster-growing halos as suggested by Chiang et al. (2017), or by a different star formation efficiency in clusters whereby a galaxy is more luminous at a fixed halo mass (Y.-K. Chiang, in private communication). Alternatively, it is also possible that protocluster LAEs simply have different ages and/or metallicity than elsewhere; however, the overall similarities in observed colors and EWs in the two environmental bins studied here argues agains this possibility.

Our result is seemingly at odds with some of the existing studies which found that galaxies in dense environment largely grow at a similar rate as those in average fields (Lemaux et al. 2018a; Shi et al. 2019), perhaps with an exception at the massive end (e.g., Lemaux et al. 2014). However, it is worth noting that these studies focused on more UV-luminous, LBG-like galaxies that are, on average, a factor of $\gtrsim 5 - 10$ more massive than the LAE population studied in this work. To discern a clearer trend and to study how it depends on galaxy's luminosity and stellar mass, and on galaxy types (LBGs, LAEs, etc.), a more comprehensive study is needed.

We speculate a potential implication of our result in the cosmological context. By following the structures identified as cluster-sized dark matter halos at $z = 0$ in the Millennium simulations, Chiang et al. (2017) estimated that the fractional contribution to the total star formation rate density (SFRD) from galaxies that will end up in clusters increases dramatically with redshift, from only a few percent at $z = 0.5 - 1.0$, to ≈ 20–30% at $z = 2 - 4$, and to nearly 50% at $z > 8$. This change is mainly driven by large cosmic volumes occupied by protoclusters well before their final coalescence (see their Figure 1) as well as high galaxy overdensities and the top-heavy halo mass function therein (Chiang et al. 2017).

If the observed higher luminosity of protocluster LAEs has an astrophysical origin (e.g., a higher efficiency in converting gas into stars) rather than a cosmological one, it would follow that the total contribution to the cos-mic SFRD from protoclusters would be even greater than the Chiang et al. (2017) estimate. Separating out these effects will be challenging, however, and will require a much larger sample of protoclusters and a better characterization of halo statistics in different environments.

5.4. Search of progenitors of a brightest cluster galaxy

Brightest cluster galaxies (BCGs) are the most massive galaxies in galaxy clusters. In the local universe, they are typically elliptical galaxies residing near the cluster center defined by X-ray emission peak (e.g., Lin & Mohr 2004). Identification and characterization of their progenitors ('proto-BCGs') at high redshift would illuminate the early stages of their formation.

At $z \sim 3$, the rest-frame optical/near-IR luminosity $(0.5-1.6\mu m)$ tracing the total stellar content is redshifted into the K_S band and beyond. Thus, the most effective search should be based on the photometric properties at infrared wavelengths. Although the D1 field was imaged in the near-IR JHK_S bands by the WIRCam Deep Survey (Bielby et al. 2012), the newly discovered galaxy overdensities unfortunately lie near the edge of its coverage (see their Figure 2 for the coverage map). $\approx 20\%$ of the area enclosing the 'A' and 'B+C' structures has no K_S band coverage while an additional 10% of the area has only partial coverage (<50% of the full exposure 4.7 hr).

Given this limitation, we caution that any search based on the existing data would be severely limited by the depth and areal coverage in obtaining a complete census of massive galaxies in this structure. While a more comprehensive search of massive galaxies in this region based on the *Spitzer* IRAC 3.6μm detection will be presented in the future (J. Toshikawa et al., in prep, K. Shi et al., in prep), in this work, we base our proto-BCG search on our existing LBG catalog instead, focusing on UV-luminous galaxies that already have a large stellar content. We require that a given galaxy must have the r-band magnitude $r \leq 24$ (roughly corresponding to $\gtrsim 1.6L^*_{\mathrm{UV},z\sim3}$: Reddy & Steidel 2009). In addition, to further constrain its stellar mass, it should also be well detected in the K_S band catalog. A total of 80 galaxies satisfy these

criteria corresponding to a surface density of 0.06±0.01 arcmin^{-2}.

In the left panel of Figure 9, we show the $J - K_S$ colors vs K_S band magnitudes for all selected sources. The majority have $K_S > 22.5$ and relatively blue $J - K_S$ colors. Using the EZGal software (Mancone & Gonzalez 2012), we also compute the expected color and luminosity evolution assuming several different star formation histories. The Bruzual & Charlot (2003) stellar population synthesis models and local starburst-like dust reddening curve (Calzetti et al. 2000) are adopted for the calculation. The model magnitudes are normalized to a lower redshift ($z = 1.8$) $M_\star$ cluster galaxy in the 3.6μm band (Mancone et al. 2010), assuming passive evolution from $z \sim 3.1$ to $z \sim 1.8$. The model tracks represent the time evolution of the galaxy.

Of the 80 galaxies, only four reside in the combined LBG and LAE overdensity region. The area covered by the WIRDS data is 93.7 arcmin^2, and thus the expected number therein is 6 ± 2. The K_S-brightest galaxy ($K_S = 21.05$), which we dub G411155, is shown as a red circle in the left panel of Figure 9. Its location is also marked in Figure 6 (red diamond). G411155 is the reddest LBG in the entire field ($J - K_S = 1.92$), and would easily meet a typical color selection for distant red galaxies (DRGs) at high redshift ($J - K_S > 1.4$: Franx et al. 2003; van Dokkum et al. 2003). G411155 is very bright in the IRAC 8μm and the MIPS 24μm bands, having the flux densities of 0.13 mJy and 1.43 mJy, respectively. The remaining three galaxies have relatively modest K_S band brightness ($K_S = 23-24$) and are bluer ($J - K_S < 1.4$). None of the five galaxies has a X-ray or radio counterpart (Bondi et al. 2003; Chiappetti et al. 2005).

Using the Bielby et al. (2012) and Lonsdale et al. (2003) catalogs, we extract the multi-wavelength photometry ($ugrizJHK_S[3.6][4.5][5.8][8.0][24][70][160]$) of G411155 using the Kron-like total fluxes. We perform the SED fitting with the CIGALE software (Noll et al. 2009; Boquien et al. 2018) using both galaxy and AGN templates. Star formation histories are modeled as an exponentially declining function with the characteristic timescale τ values of 100 Myr to 1 Gyr. AGN models from Fritz et al. (2006) are used as templates.

In Figure 9 (right), we show the best-fit SED model together with the photometric measurements. In the inset, we also show the photometric redshift probability density which peaks at $z \sim 3.1$. The best-fit physical parameters suggest that G411155 has a short star-forming time scale with the luminosity-weighted age of ≈200 Myr. The model fit also suggests a dust-obscured AGN component which dominates the infrared energy budget: 70% of the total IR luminosity originates from the AGN. The galaxy is already ultramassive at $M_{star} \approx 2 \times 10^{11} M_\odot$, and it continues to form stars at a rate SFR $\sim 500 M_\odot \mathrm{yr}^{-1}$!

We compare our proto-BCG candidate with those found in the literature. Lemaux et al. (2014) identified a proto-BCG candidate in a $z \sim 3.3$ protocluster. It contains a powerful Type I AGN (relatively unobscured by dust with broad lines) with a K_S band magnitude of 20.67 ($z - K_S = 0.1$) with the estimated stellar mass and age of $\sim 8 \times 10^{10} M_\odot$ and ~ 300 Myr. The SFR inferred from the total IR luminosity is $\sim 750 \ M_\odot \mathrm{yr}^{-1}$. Although

we do not have a spectrum for G411155, these two proto-BCG candidates have comparable physical properties.

Near the center of a protocluster at $z = 3.09$, Kubo et al. (2015, 2016) discovered a dense group of massive galaxies consisting of seven K_S bright ($K_S \sim 22 - 24$) and red galaxies ($J - K_S > 1.1$) with a combined stellar mass of $\approx 6 \times 10^{11} M_\odot$. They argued that the group is likely in the merger phase which will evolve into a BCG observed in the local universe. Wang et al. (2016) reported an overdensity of 11 massive ($\gtrsim 10^{11} M_\odot$) DRGs within a compact core (80 kpc) in another $z = 2.51$ structure, and speculated that their findings may signify a rapid buildup of a cluster core. Identifying and studying similar systems in a larger sample of protoclusters will elucidate evolutionary stages of cluster BCGs.

Finally, G411155 lies very close to the spectroscopic sources at $z = 3.13$, in particular four sources two of which are also LAEs, as illustrated in Figure 4.1. Given its photometric redshift (see inset of Figure 9), it is possible that these galaxies are members of the same group, which is falling towards the center of its parent halo located at a projected distance ≈1 Mpc (physical) away from it. Given its optical brightness, it should be relatively easy to measure its redshift and thereby unambiguously determine its physical association with these sources.

6. SUMMARY

In this paper, we initially set out to investigate a large-scale structure around a significant LBG overdensity in the CFHTLS D1 field. A subset of these galaxies were targeted by Toshikawa et al. (2016), and five are confirmed to lie at $z_{\mathrm{spec}} = 3.13$. At this redshift, Lyα emission is conveniently redshifted into a zero-redshift [O III] filter, providing a rare opportunity to examine how the same structure is populated by galaxies of different spectral types, thereby evaluating the efficiency of different search techniques for high-redshift protoclusters. To this end, we have obtained new deep observations using the Mosaic $o3$ filter; by combining the data with the existing broad-band observations, 93 LAE candidates are identified at $z = 3.11 - 3.15$.

The angular distribution of these LAEs is clearly non-uniform, revealing a prominent overdensity at the western end of the field containing 21 galaxies along with a luminous Lyα nebula. The angular size and level of the LAE overdensity are consistent with those observed for several confirmed protoclusters. However, our comparison of the LAE and LBG distributions has resulted in a surprising discovery: the LAE-rich region is spatially offset by ∼15 Mpc from the LBG-rich region. In the latter, there is a general dearth of LAEs while the LAE overdensity is also populated by LBG candidates. Our findings paint a more complex picture of cluster formation in which the halo assembly bias may play a significant role in determining a dominant type of galaxy constituents therein. Based on our investigations, we conclude the following:

- We report a significant LAE overdensity located 10′ south of the five spectroscopic sources at $z = 3.13$. The observed surface density therein is higher than that expected in an average field by a factor of 3.3 ± 0.9. The total mass enclosed in the overdensity is estimated to
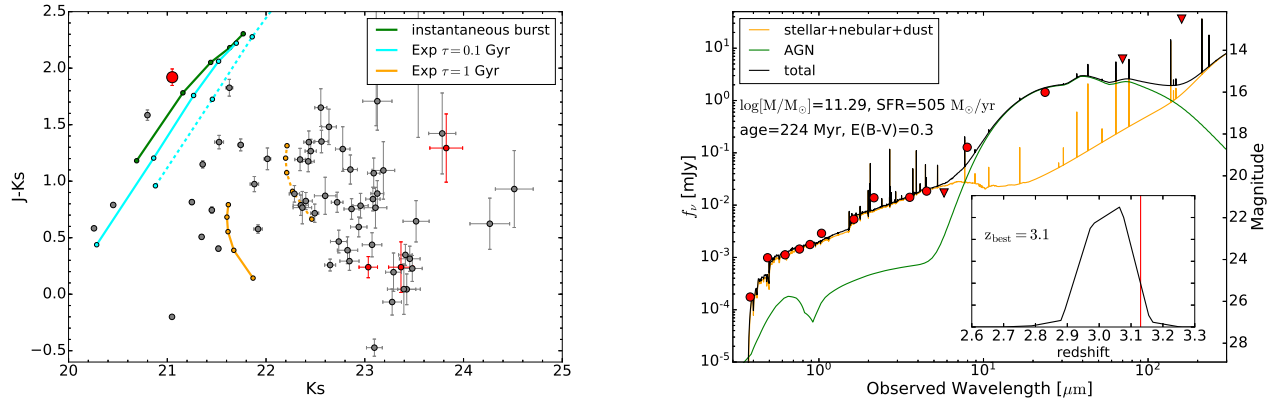
Fig. 9.— *Left:* A color-magnitude diagram of UV-luminous LBGs with K_S band detection ($r \le 24$: grey circles). The proto-BCG candidate, G411155 (large red circle), is the reddest LBG and also one of the brightest in the K_S band. Three other LBGs near the LAE/LBG overdensities are shown as smaller red circles. Colored lines represent galaxies that formed through an instantaneous burst (green), and with an exponentially declining SF history with τ values of 100 Myr (cyan) and 1 Gyr (yellow); all are observed at $z = 3.1$ with the population age of 0.2 Gyr (bottom) to 1.0 Gyr with a stepsize of 0.2 Gyr. For the exponentially declining models, we also show the color tracks assuming the reddening $E(B - V) = 0.2$ as dashed lines. *Right:* The best-fit SED model of G411155 is shown in black together with the photometric measurements (red symbols) and best-fit parameters. The galaxy (stars+gas+dust) and AGN components are shown in orange and green, respectively. In the inset, we show the photometric redshift probability density. The red vertical line marks $z = 3.13$, the redshift of the spectroscopic sources within the LBG overdensity.

be $M_{\rm tot} \approx (1.0 - 1.5) \times 10^{15} M_\odot$, implying that the LAE overdensity traces a massive structure that will evolve into a galaxy cluster similar to the present-day Coma.

- We analyze the LBG overdensity based on the existing deep broad-band observations to evaluate its significance and contemplate on its possible relationship with the LAE-traced protocluster. Given the angular extent and the level of overdensity, we conclude that it will also evolve into a Coma-sized galaxy cluster.

- If the spatial segregation of the LAE and LBG-rich structures is interpreted as a manifestation of the halo assembly bias, it follows that different search techniques would be biased accordingly to the formation age of the host halo. Similar selection biases are expected if more massive and relaxed halos preferentially host more evolved galaxies such as LBGs. With multiple upcoming wide-field surveys will be targeting both types of galaxies (e.g., Hobby-Eberly telescope dark energy experiment, Large synoptic survey telescope), testing this hypothesis will be within reach in the next decade. Such studies will lead us to deeper understanding of early stages of galaxy formation in dense cluster environments, and help us optimize search techniques to reliably identify and study progenitors of massive galaxy clusters.

- We find tentative evidence that the median SFR is higher for Lyα-emitting galaxies in protocluster environment. When our LAE candidates are split accordingly to their 2D environment, the LAEs residing in the overdensity consistently have larger Lyα and UV luminosities – by $\sim 40\%$ and $\sim 70\%$, respectively – than the rest, in agreement with our previous study based on another protocluster (Dey et al. 2016a). The enhancement appears to be widespread within the overdensity region with no clear radial dependence. The difference cannot be explained by the galaxy overdensity alone, and may require either a top-heavy mass function or a higher star formation efficiency for protocluster

halos. However, we cannot rule out the possibility that the trend is produced by a deficit of low-luminosity low-mass galaxies in protocluster environment.

- Our search for Lyα nebulae in the entire field yields a single nebula with the total Lyα luminosity $\approx 2 \times 10^{43}$ erg s^{-1} and the half-light radius (assuming an exponentially declining profile) of at least $5''$ (39 kpc at $z = 3.13$). Its location at the outer edge of the LAE overdensity may support a physical picture advocated by Bădescu et al. (2017), that Lyα nebulae trace group-sized halos falling in towards the protocluster center. The large variations seen in the observed number of Lyα nebulae around protoclusters hint at the short-lived nature of the phenomenon, perhaps brought on by galaxy-galaxy interactions.

- We have also identified a brightest cluster galaxy candidate located $\approx 2'$ from the center of the LBG overdensity. The galaxy is one of the brightest LBGs in our sample, and has already assembled a stellar mass of $\approx 2 \times 10^{11} M_\odot$. A full SED modeling suggests that a highly dust-obscured AGN dominates its mid-infrared flux at $\lambda_{\rm obs} \gtrsim 8\mu$m while still active star formation is responsible for a fairly reddened rest-frame UV and optical part of its SED. While the AGN-driven quenching of star formation in an already massive cluster galaxy fits the general expectation of how and when cluster galaxies formed, further validation (i.e., high spatial resolution imaging and a spectroscopic redshift) is needed to determine whether it is physically associated with the galaxy overdensity.

REFERENCES

Alberts, S., Pope, A., Brodwin, M., Atlee, D. W., Lin, Y.-T., Dey, A., Eisenhardt, P. R. M., Gettings, D. P., Gonzalez, A. H., Jannuzi, B. T., Mancone, C. L., Moustakas, J., Snyder, G. F., Stanford, S. A., Stern, D., Weiner, B. J., & Zeimann, G. R. 2014, MNRAS, 437, 437

Bertin, E. & Arnouts, S. 1996, A&AS, 117, 393

Bielby, R., Hill, M. D., Shanks, T., Crighton, N. H. M., Infante, L., Bornancini, C. G., Francke, H., Héraudeau, P., Lambas, D. G., Metcalfe, N., Minniti, D., Padilla, N., Theuns, T., Tummuangpak, P., & Weilbacher, P. 2013, MNRAS, 430, 425

Bielby, R., Hudelot, P., McCracken, H. J., Ilbert, O., Daddi, E., Le Fèvre, O., Gonzalez-Perez, V., Kneib, J.-P., Marmo, C., Mellier, Y., Salvato, M., Sanders, D. B., & Willott, C. J. 2012, A&A, 545, A23

Bondi, M., Ciliegi, P., Zamorani, G., Gregorini, L., Vettolani, G., Parma, P., de Ruiter, H., Le Fevre, O., Arnaboldi, M., Guzzo, L., Maccagni, D., Scaramella, R., Adami, C., Bardelli, S., Bolzonella, M., Bottini, D., Cappi, A., Foucaud, S., Franzetti, P., Garilli, B., Gwyn, S., Ilbert, O., Iovino, A., Le Brun, V., Marano, B., Marinoni, C., McCracken, H. J., Meneux, B., Pollo, A., Pozzetti, L., Radovich, M., Ripepi, V., Rizzo, D., Scodeggio, M., Tresse, L., Zanichelli, A., & Zucca, E. 2003, A&A, 403, 857

Boquien, M., Burgarella, D., Roehlly, Y., Buat, V., Ciesla, L., Corre, D., Inoue, A. K., & Salas, H. 2018, arXiv e-prints, arXiv:1811.03094

Bower, R. G., Lucey, J. R., & Ellis, R. S. 1992, MNRAS, 254, 601

Bridge, C. R., Blain, A., Borys, C. J. K., Petty, S., Benford, D., Eisenhardt, P., Farrah, D., Griffith, R. L., Jarrett, T., Lonsdale, C., Stanford, S. A., Stern, D., Tsai, C.-W., Wright, E. L., & Wu, J. 2013, ApJ, 769, 91

Brodwin, M., Stanford, S. A., Gonzalez, A. H., Zeimann, G. R., Snyder, G. F., Mancone, C. L., Pope, A., Eisenhardt, P. R., Stern, D., Alberts, S., Ashby, M. L. N., Brown, M. J. I., Chary, R.-R., Dey, A., Galametz, A., Gettings, D. P., Jannuzi, B. T., Miller, E. D., Moustakas, J., & Moustakas, L. A. 2013, ApJ, 779, 138

Bruzual, G. & Charlot, S. 2003, MNRAS, 344, 1000

Bădescu, T., Yang, Y., Bertoldi, F., Zabludoff, A., Karim, A., & Magnelli, B. 2017, ApJ, 845, 172

Calzetti, D., Armus, L., Bohlin, R. C., Kinney, A. L., Koornneef, J., & Storchi-Bergmann, T. 2000, ApJ, 533, 682

Chiang, Y.-K., Overzier, R., & Gebhardt, K. 2013, ApJ, 779, 127

Chiang, Y.-K., Overzier, R. A., Gebhardt, K., & Henriques, B. 2017, ApJ, 844, L23

Chiappetti, L., Tajer, M., Trinchieri, G., Maccagni, D., Maraschi, L., Paioro, L., Pierre, M., Surdej, J., Garcet, O., Gosset, E., Le Fèvre, O., Bertin, E., McCracken, H. J., Mellier, Y., Foucaud, S., Radovich, M., Ripepi, V., & Arnaboldi, M. 2005, A&A, 439, 413

Ciardullo, R., Gronwall, C., Adams, J. J., Blanc, G. A., Gebhardt, K., Finkelstein, S. L., Jogee, S., Hill, G. J., Drory, N., Hopp, U., Schneider, D. P., Zeimann, G. R., & Dalton, G. B. 2013, ApJ, 769, 83

Coleman, G. D., Wu, C.-C., & Weedman, D. W. 1980, ApJS, 43, 393

Cooke, E. A., Hatch, N. A., Muldrew, S. I., Rigby, E. E., & Kurk, J. D. 2014, MNRAS, 440, 3262

Cooper, M. C., Newman, J. A., Madgwick, D. S., Gerke, B. F., Yan, R., & Davis, M. 2005, ApJ, 634, 833

Cooper, M. C., Newman, J. A., Weiner, B. J., Yan, R., Willmer, C. N. A., Bundy, K., Coil, A. L., Conselice, C. J., Davis, M., Faber, S. M., Gerke, B. F., Guhathakurta, P., Koo, D. C., & Noeske, K. G. 2008, MNRAS, 383, 1058

Cucciati, O., Lemaux, B. C., Zamorani, G., Le Fèvre, O., Tasca, L. A. M., Hathi, N. P., Lee, K.-G., Bardelli, S., Cassata, P., Garilli, B., Le Brun, V., Maccagni, D., Pentericci, L., Thomas, R., Vanzella, E., Zucca, E., Lubin, L. M., Amorin, R., Cassarà, L. P., Cimatti, A., Talia, M., Vergani, D., Koekemoer, A., Pforr, J., & Salvato, M. 2018, A&A, 619, A49

Cucciati, O., Zamorani, G., Lemaux, B. C., Bardelli, S., Cimatti, A., Le Fèvre, O., Cassata, P., Garilli, B., Le Brun, V., Maccagni, D., Pentericci, L., Tasca, L. A. M., Thomas, R., Vanzella, E., Zucca, E., Amorin, R., Capak, P., Cassarà, L. P., Castellano, M., Cuby, J. G., de la Torre, S., Durkalec, A., Fontana, A., Giavalisco, M., Grazian, A., Hathi, N. P., Ilbert, O., Moreau, C., Paltani, S., Ribeiro, B., Salvato, M., Schaerer, D., Scodeggio, M., Sommariva, V., Talia, M., Taniguchi, Y., Tresse, L., Vergani, D., Wang, P. W., Charlot, S., Contini, T., Fotopoulou, S., López- Sanjuan, C., Mellier, Y., & Scoville, N. 2014, A&A, 570, A16

Dey, A., Bian, C., Soifer, B. T., Brand, K., Brown, M. J. I., Chaffee, F. H., Le Floc'h, E., Hill, G., Houck, J. R., Jannuzi, B. T., Rieke, M., Weedman, D., Brodwin, M., & Eisenhardt, P. 2005, ApJ, 629, 654

Dey, A., Lee, K.-S., Reddy, N., Cooper, M., Inami, H., Hong, S., Gonzalez, A. H., & Jannuzi, B. T. 2016a, ApJ, 823, 11

Dey, A., Rabinowitz, D., Karcher, A., Bebek, C., Baltay, C., Sprayberry, D., Valdes, F., Stupak, B., Donaldson, J., Emmet, W., Hurteau, T., Abareshi, B., Marshall, B., Lang, D., Fitzpatrick, M., Daly, P., Joyce, D., Schlegel, D., Schweiker, H., Allen, L., Blum, B., & Levi, M. 2016b, in Proc. SPIE, Vol. 9908, Ground-based and Airborne Instrumentation for Astronomy VI, 99082C

Dressler, A. 1980, ApJ, 236, 351

Eisenhardt, P. R. M., Brodwin, M., Gonzalez, A. H., Stanford, S. A., Stern, D., Barmby, P., Brown, M. J. I., Dawson, K., Dey, A., Doi, M., Galametz, A., Jannuzi, B. T., Kochanek, C. S., Meyers, J., Morokuma, T., & Moustakas, L. A. 2008, ApJ, 684, 905

Elbaz, D., Daddi, E., Le Borgne, D., Dickinson, M., Alexander, D. M., Chary, R.-R., Starck, J.-L., Brandt, W. N., Kitzbichler, M., MacDonald, E., Nonino, M., Popesso, P., Stern, D., & Vanzella, E. 2007, A&A, 468, 33

Erb, D. K., Bogosavljević, M., & Steidel, C. C. 2011, ApJ, 740, L31

Fasano, G. & Franceschini, A. 1987, MNRAS, 225, 155

Finkelstein, S. L., Hill, G. J., Gebhardt, K., Adams, J., Blanc, G. A., Papovich, C., Ciardullo, R., Drory, N., Gawiser, E., Gronwall, C., Schneider, D. P., & Tran, K.-V. 2011, ApJ, 729, 140

Franx, M., Labbé, I., Rudnick, G., van Dokkum, P. G., Daddi, E., Förster Schreiber, N. M., Moorwood, A., Rix, H.-W., Röttgering, H., van der Wel, A., van der Werf, P., & van Starkenburg, L. 2003, ApJ, 587, L79

Fritz, J., Franceschini, A., & Hatziminaoglou, E. 2006, MNRAS, 366, 767

Gao, L., Springel, V., & White, S. D. M. 2005, MNRAS, 363, L66

Gawiser, E., Francke, H., Lai, K., Schawinski, K., Gronwall, C., Ciardullo, R., Quadri, R., Orsi, A., Barrientos, L. F., Blanc, G. A., Fazio, G., Feldmeier, J. J., Huang, J.-s., Infante, L., Lira, P., Padilla, N., Taylor, E. N., Treister, E., Urry, C. M., van Dokkum, P. G., & Virani, S. N. 2007, ApJ, 671, 278

Gawiser, E., van Dokkum, P. G., Gronwall, C., Ciardullo, R., Blanc, G. A., Castander, F. J., Feldmeier, J., Francke, H., Franx, M., Haberzettl, L., Herrera, D., Hickey, T., Infante, L., Lira, P., Maza, J., Quadri, R., Richardson, A., Schawinski, K., Schirmer, M., Taylor, E. N., Treister, E., Urry, C. M., & Virani, S. N. 2006, ApJ, 642, L13

Goto, T., Yamauchi, C., Fujita, Y., Okamura, S., Sekiguchi, M., Smail, I., Bernardi, M., & Gomez, P. L. 2003, MNRAS, 346, 601

Gronwall, C., Ciardullo, R., Hickey, T., Gawiser, E., Feldmeier, J. J., van Dokkum, P. G., Urry, C. M., Herrera, D., Lehmer, B. D., Infante, L., Orsi, A., Marchesini, D., Blanc, G. A., Francke, H., Lira, P., & Treister, E. 2007, ApJ, 667, 79

Guaita, L., Acquaviva, V., Padilla, N., Gawiser, E., Bond, N. A., Ciardullo, R., Treister, E., Kurczynski, P., Gronwall, C., Lira, P., & Schawinski, K. 2011, ApJ, 733, 114

Guaita, L., Gawiser, E., Padilla, N., Francke, H., Bond, N. A., Gronwall, C., Ciardullo, R., Feldmeier, J. J., Sinawa, S., Blanc, G. A., & Virani, S. 2010, ApJ, 714, 255

Gwyn, S. D. J. 2012, AJ, 143, 38

Hatch, N. A., Kurk, J. D., Pentericci, L., Venemans, B. P., Kuiper, E., Miley, G. K., & Röttgering, H. J. A. 2011, MNRAS, 415, 2993

Hathi, N. P., Le Fèvre, O., Ilbert, O., Cassata, P., Tasca, L. A. M., Lemaux, B. C., Garilli, B., Le Brun, V., Maccagni, D., Pentericci, L., Thomas, R., Vanzella, E., Zamorani, G., Zucca, E., Amorín, R., Bardelli, S., Cassarà, L. P., Castellano, M., Cimatti, A., Cucciati, O., Durkalec, A., Fontana, A., Giavalisco, M., Grazian, A., Guaita, L., Koekemoer, A., Paltani, S., Pforr, J., Ribeiro, B., Schaerer, D., Scodeggio, M., Sommariva, V., Talia, M., Tresse, L., Vergani, D., Capak, P., Charlot, S., Contini, T., Cuby, J. G., de la Torre, S., Dunlop, J., Fotopoulou, S., López-Sanjuan, C., Mellier, Y., Salvato, M., Scoville, N., Taniguchi, Y., & Wang, P. W. 2016, A&A, 588, A26

Higuchi, R., Ouchi, M., Ono, Y., Shibuya, T., Toshikawa, J., Harikane, Y., Kojima, T., Chiang, Y.-K., Egami, E., Kashikawa, N., Overzier, R., Konno, A., Inoue, A. K., Hasegawa, K., Fujimoto, S., Goto, T., Ishikawa, S., Ito, K., Komiyama, Y., & Tanaka, M. 2018, arXiv e-prints, arXiv:1801.00531

Hogg, D. W., Cohen, J. G., Blandford, R., & Pahre, M. A. 1998, ApJ, 504, 622

Husband, K., Bremer, M. N., Stott, J. P., & Murphy, D. N. A. 2016, MNRAS, 462, 421

Jiang, L., Wu, J., Bian, F., Chiang, Y.-K., Ho, L. C., Shen, Y., Zheng, Z.-Y., Bailey, J. I., Blanc, G. A., Crane, J. D., Fan, X., Mateo, M., Olszewski, E. W., Oyarzún, G. A., Wang, R., & Wu, X.-B. 2018, Nature Astronomy, 2, 962

Kennicutt, Jr., R. C. 1998, ARA&A, 36, 189

Komatsu, E., Smith, K. M., Dunkley, J., Bennett, C. L., Gold, B., Hinshaw, G., Jarosik, N., Larson, D., Nolta, M. R., Page, L., Spergel, D. N., Halpern, M., Hill, R. S., Kogut, A., Limon, M., Meyer, S. S., Odegard, N., Tucker, G. S., Weiland, J. L., Wollack, E., & Wright, E. L. 2011, ApJS, 192, 18

Koyama, Y., Smail, I., Kurk, J., Geach, J. E., Sobral, D., Kodama, T., Nakata, F., Swinbank, A. M., Best, P. N., Hayashi, M., & Tadaki, K.-i. 2013, MNRAS, 434, 423

Kubo, J. M., Stebbins, A., Annis, J., Dell'Antonio, I. P., Lin, H., Khiabanian, H., & Frieman, J. A. 2007, ApJ, 671, 1466

Kubo, M., Yamada, T., Ichikawa, T., Kajisawa, M., Matsuda, Y., & Tanaka, I. 2015, ApJ, 799, 38

Kubo, M., Yamada, T., Ichikawa, T., Kajisawa, M., Matsuda, Y., Tanaka, I., & Umehata, H. 2016, MNRAS, 455, 3333

Kuiper, E., Hatch, N. A., Venemans, B. P., Miley, G. K., Röttgering, H. J. A., Kurk, J. D., Overzier, R. A., Pentericci, L., Bland-Hawthorn, J., & Cepa, J. 2011, MNRAS, 417, 1088

Kurk, J. D., Pentericci, L., Röttgering, H. J. A., & Miley, G. K. 2004, A&A, 428, 793

Kurk, J. D., Röttgering, H. J. A., Pentericci, L., Miley, G. K., van Breugel, W., Carilli, C. L., Ford, H., Heckman, T., McCarthy, P., & Moorwood, A. 2000a, A&A, 358, L1

—. 2000b, A&A, 358, L1

Le Fèvre, O., Cassata, P., Cucciati, O., Garilli, B., Ilbert, O., Le Brun, V., Maccagni, D., Moreau, C., Scodeggio, M., Tresse, L., Zamorani, G., Adami, C., Arnouts, S., Bardelli, S., Bolzonella, M., Bondi, M., Bongiorno, A., Bottini, D., Cappi, A., Charlot, S., Ciliegi, P., Contini, T., de la Torre, S., Foucaud, S., Franzetti, P., Gavignaud, I., Guzzo, L., Iovino, A., Lemaux, B., López-Sanjuan, C., McCracken, H. J., Marano, B., Marinoni, C., Mazure, A., Mellier, Y., Merighi, R., Merluzzi, P., Paltani, S., Pellò, R., Pollo, A., Pozzetti, L., Scaramella, R., Tasca, L., Vergani, D., Vettolani, G., Zanichelli, A., & Zucca, E. 2013, A&A, 559, A14

Le Fèvre, O., Tasca, L. A. M., Cassata, P., Garilli, B., Le Brun, V., Maccagni, D., Pentericci, L., Thomas, R., Vanzella, E., Zamorani, G., Zucca, E., Amorin, R., Bardelli, S., Capak, P., Cassarà, L., Castellano, M., Cimatti, A., Cuby, J. G., Cucciati, O., de la Torre, S., Durkalec, A., Fontana, A., Giavalisco, M., Grazian, A., Hathi, N. P., Ilbert, O., Lemaux, B. C., Moreau, C., Paltani, S., Ribeiro, B., Salvato, M., Schaerer, D., Scodeggio, M., Sommariva, V., Talia, M., Taniguchi, Y., Tresse, L., Vergani, D., Wang, P. W., Charlot, S., Contini, T., Fotopoulou, S., López-Sanjuan, C., Mellier, Y., & Scoville, N. 2015, A&A, 576, A79

Lee, K.-S., Dey, A., Hong, S., Reddy, N., Wilson, C., Jannuzi, B. T., Inami, H., & Gonzalez, A. H. 2014, ApJ, 796, 126

Lee, K.-S., Ferguson, H. C., Wiklind, T., Dahlen, T., Dickinson, M. E., Giavalisco, M., Grogin, N., Papovich, C., Messias, H., Guo, Y., & Lin, L. 2012, ApJ, 752, 66

Lemaux, B. C., Cucciati, O., Tasca, L. A. M., Le Fèvre, O., Zamorani, G., Cassata, P., Garilli, B., Le Brun, V., Maccagni, D., Pentericci, L., Thomas, R., Vanzella, E., Zucca, E., Amorín, R., Bardelli, S., Capak, P., Cassarà, L. P., Castellano, M., Cimatti, A., Cuby, J. G., de la Torre, S., Durkalec, A., Fontana, A., Giavalisco, M., Grazian, A., Hathi, N. P., Ilbert, O., Moreau, C., Paltani, S., Ribeiro, B., Salvato, M., Schaerer, D., Scodeggio, M., Sommariva, V., Talia, M., Taniguchi, Y., Tresse, L., Vergani, D., Wang, P. W., Charlot, S., Contini, T., Fotopoulou, S., Gal, R. R., Kocevski, D. D., López-Sanjuan, C., Lubin, L. M., Mellier, Y., Sadibekova, T., & Scoville, N. 2014, A&A, 572, A41

Lemaux, B. C., Le Fèvre, O., Cucciati, O., Ribeiro, B., Tasca, L. A. M., Zamorani, G., Ilbert, O., Thomas, R., Bardelli, S., Cassata, P., Hathi, N. P., Pforr, J., Smolčić, V., Delvecchio, I., Novak, M., Berta, S., McCracken, H. J., Koekemoer, A., Amorín, R., Garilli, B., Maccagni, D., Schaerer, D., & Zucca, E. 2018a, A&A, 615, A77

Lemaux, B. C., Tomczak, A. R., Lubin, L. M., Gal, R. R., Shen, L., Pelliccia, D., Wu, P.-F., Hung, D., Mei, S., Le Fèvre, O., Rumbaugh, N., Kocevski, D. D., & Squires, G. K. 2018b, arXiv e-prints

Li, Y., Mo, H. J., & Gao, L. 2008, MNRAS, 389, 1419

Lin, Y.-T. & Mohr, J. J. 2004, ApJ, 617, 879

Lonsdale, C. J., Smith, H. E., Rowan-Robinson, M., Surace, J., Shupe, D., Xu, C., Oliver, S., Padgett, D., Fang, F., Conrow, T., Franceschini, A., Gautier, N., Griffin, M., Hacking, P., Masci, F., Morrison, G., O'Linger, J., Owen, F., Pérez-Fournon, I., Pierre, M., Puetter, R., Stacey, G., Castro, S., Polletta, M. d. C., Farrah, D., Jarrett, T., Frayer, D., Siana, B., Babbedge, T., Dye, S., Fox, M., Gonzalez-Solares, E., Salaman, M., Berta, S., Condon, J. J., Dole, H., & Serjeant, S. 2003, PASP, 115, 897

Madau, P. 1995, ApJ, 441, 18

Mancone, C. L. & Gonzalez, A. H. 2012, Publications of the Astronomical Society of the Pacific, 124, 606

Mancone, C. L., Gonzalez, A. H., Brodwin, M., Stanford, S. A., Eisenhardt, P. R. M., Stern, D., & Jones, C. 2010, ApJ, 720, 284

Marinoni, C., Davis, M., Newman, J. A., & Coil, A. L. 2002, ApJ, 580, 122

Matsuda, Y., Yamada, T., Hayashino, T., Tamura, H., Yamauchi, R., Ajiki, M., Fujita, S. S., Murayama, T., Nagao, T., Ohta, K., Okamura, S., Ouchi, M., Shimasaku, K., Shioya, Y., & Taniguchi, Y. 2004, AJ, 128, 569

Matsuda, Y., Yamada, T., Hayashino, T., Tamura, H., Yamauchi, R., Murayama, T., Nagao, T., Ohta, K., Okamura, S., Ouchi, M., Shimasaku, K., Shioya, Y., & Taniguchi, Y. 2005, ApJ, 634, L125

Mauduit, J.-C., Lacy, M., Farrah, D., Surace, J. A., Jarvis, M., Oliver, S., Maraston, C., Vaccari, M., Marchetti, L., Zeimann, G., Gonzáles-Solares, E. A., Pforr, J., Petric, A. O., Henriques, B., Thomas, P. A., Afonso, J., Rettura, A., Wilson, G., Falder, J. T., Geach, J. E., Huynh, M., Norris, R. P., Seymour, N., Richards, G. T., Stanford, S. A., Alexander, D. M., Becker, R. H., Best, P. N., Bizzocchi, L., Bonfield, D., Castro, N., Cava, A., Chapman, S., Christopher, N., Clements, D. L., Covone, G., Dubois, N., Dunlop, J. S., Dyke, E., Edge, A., Ferguson, H. C., Foucaud, S., Franceschini, A., Gal, R. R., Grant, J. K., Grossi, M., Hatziminaoglou, E., Hickey, S., Hodge, J. A., Huang, J.-S., Ivison, R. J., Kim, M., LeFevre, O., Lehnert, M., Lonsdale, C. J., Lubin, L. M., McLure, R. J., Messias, H., Martínez-Sansigre, A., Mortier, A. M. J., Nielsen, D. M., Ouchi, M., Parish, G., Perez-Fournon, I., Pierre, M., Rawlings, S., Readhead, A., Ridgway, S. E., Rigopoulou, D., Romer, A. K., Rosebloom, I. G., Rottgering, H. J. A., Rowan-Robinson, M., Sajina, A., Simpson, C. J., Smail, I., Squires, G. K., Stevens, J. A., Taylor, R., Trichas, M., Urrutia, T., van Kampen, E., Verma, A., & Xu, C. K. 2012, PASP, 124, 714

Mawatari, K., Yamada, T., Nakamura, Y., Hayashino, T., & Matsuda, Y. 2012, ApJ, 759, 133

Muldrew, S. I., Hatch, N. A., & Cooke, E. A. 2015, MNRAS, 452, 2528

Nakajima, K., Ouchi, M., Shimasaku, K., Hashimoto, T., Ono, Y., & Lee, J. C. 2013, ApJ, 769, 3

Noll, S., Burgarella, D., Giovannoli, E., Buat, V., Marcillac, D., & Muñoz-Mateos, J. C. 2009, A&A, 507, 1793

Oke, J. B. & Gunn, J. E. 1983, ApJ, 266, 713

Orsi, Á. A., Fanidakis, N., Lacey, C. G., & Baugh, C. M. 2016, MNRAS, 456, 3827

Oteo, I., Bongiovanni, A., Pérez García, A. M., Cepa, J., Ederoclite, A., Sánchez-Portal, M., Pintos-Castro, I., Pérez-Martínez, R., Berta, S., Magnelli, B., Popesso, P., Pozzi, F., Poglitsch, A., Lutz, D., Genzel, R., Tacconi, L., Förster Schreiber, N., Sturm, E., Elbaz, D., Aussel, H., Daddi, E., Andreani, P., Cimatti, A., Maiolino, R., Altieri, B., & Valtchanov, I. 2012, A&A, 541, A65

Ouchi, M., Shimasaku, K., Akiyama, M., Simpson, C., Saito, T., Ueda, Y., Furusawa, H., Sekiguchi, K., Yamada, T., Kodama, T., Kashikawa, N., Okamura, S., Iye, M., Takata, T., Yoshida, M., & Yoshida, M. 2008, ApJS, 176, 301

Overzier, R. A., Bouwens, R. J., Cross, N. J. G., Venemans, B. P., Miley, G. K., Zirm, A. W., Benítez, N., Blakeslee, J. P., Coe, D., Demarco, R., Ford, H. C., Homeier, N. L., Illingworth, G. D., Kurk, J. D., Martel, A. R., Mei, S., Oliveira, I., Röttgering, H. J. A., Tsvetanov, Z. I., & Zheng, W. 2008, ApJ, 673, 143

Palunas, P., Teplitz, H. I., Francis, P. J., Williger, G. M., & Woodgate, B. E. 2004, ApJ, 602, 545

Peacock, J. A. 1983, MNRAS, 202, 615

Pentericci, L., Kurk, J. D., Röttgering, H. J. A., Miley, G. K., van Breugel, W., Carilli, C. L., Ford, H., Heckman, T., McCarthy, P., & Moorwood, A. 2000, A&A, 361, L25

Prescott, M. K. M., Dey, A., Brodwin, M., Chaffee, F. H., Desai, V., Eisenhardt, P., Le Floc'h, E., Jannuzi, B. T., Kashikawa, N., Matsuda, Y., & Soifer, B. T. 2012, ApJ, 752, 86

Prescott, M. K. M., Kashikawa, N., Dey, A., & Matsuda, Y. 2008, ApJ, 678, L77

Reddy, N. A. & Steidel, C. C. 2009, ApJ, 692, 778

Salpeter, E. E. 1955, ApJ, 121, 161

Santos, J. S., Altieri, B., Tanaka, M., Valtchanov, I., Saintonge, A., Dickinson, M., Foucaud, S., Kodama, T., Rawle, T. D., & Tadaki, K. 2014, MNRAS, 438, 2565

Shapley, A. E., Steidel, C. C., Pettini, M., & Adelberger, K. L. 2003, ApJ, 588, 65

Shi, K., Lee, K.-S., Dey, A., Huang, Y., Malavasi, N., Hung, C.-L., Inami, H., Ashby, M., Duncan, K., Xue, R., Reddy, N., Hong, S., Jannuzi, B. T., Cooper, M. C., Gonzalez, A. H., Röttgering, H. J. A., Best, P. N., & Tasse, C. 2019, ApJ, 871, 83

Shimakawa, R., Kodama, T., Hayashi, M., Prochaska, J. X., Tanaka, I., Cai, Z., Suzuki, T. L., Tadaki, K.-i., & Koyama, Y. 2018, MNRAS, 473, 1977

Sobral, D., Santos, S., Matthee, J., Paulino-Afonso, A., Ribeiro, B., Calhau, J., & Khostovan, A. A. 2018, MNRAS, 476, 4725

Song, M., Finkelstein, S. L., Gebhardt, K., Hill, G. J., Drory, N., Ashby, M. L. N., Blanc, G. A., Bridge, J., Chonis, T., Ciardullo, R., Fabricius, M., Fazio, G. G., Gawiser, E., Gronwall, C., Hagen, A., Huang, J.-S., Jogee, S., Livermore, R., Salmon, B., Schneider, D. P., Willner, S. P., & Zeimann, G. R. 2014, ApJ, 791, 3

Springel, V., White, S. D. M., Jenkins, A., Frenk, C. S., Yoshida, N., Gao, L., Navarro, J., Thacker, R., Croton, D., Helly, J., Peacock, J. A., Cole, S., Thomas, P., Couchman, H., Evrard, A., Colberg, J., & Pearce, F. 2005, Nature, 435, 629

Steidel, C. C., Adelberger, K. L., Dickinson, M., Giavalisco, M., Pettini, M., & Kellogg, M. 1998, ApJ, 492, 428

Steidel, C. C., Adelberger, K. L., Shapley, A. E., Erb, D. K., Reddy, N. A., & Pettini, M. 2005, ApJ, 626, 44

Steidel, C. C., Adelberger, K. L., Shapley, A. E., Pettini, M., Dickinson, M., & Giavalisco, M. 2000, ApJ, 532, 170

Steidel, C. C., Bogosavljević, M., Shapley, A. E., Kollmeier, J. A., Reddy, N. A., Erb, D. K., & Pettini, M. 2011, ApJ, 736, 160

Toshikawa, J., Kashikawa, N., Ota, K., Morokuma, T., Shibuya, T., Hayashi, M., Nagao, T., Jiang, L., Malkan, M. A., Egami, E., Shimasaku, K., Motohara, K., & Ishizaki, Y. 2012, ApJ, 750, 137

Toshikawa, J., Kashikawa, N., Overzier, R., Malkan, M. A., Furusawa, H., Ishikawa, S., Onoue, M., Ota, K., Tanaka, M., Niino, Y., & Uchiyama, H. 2016, ApJ, 826, 114

Toshikawa, J., Uchiyama, H., Kashikawa, N., Ouchi, M., Overzier, R., Ono, Y., Harikane, Y., Ishikawa, S., Kodama, T., Matsuda, Y., Lin, Y.-T., Onoue, M., Tanaka, M., Nagao, T., Akiyama, M., Komiyama, Y., Goto, T., & Lee, C.-H. 2018, PASJ, 70, S12

Tran, K.-V. H., Papovich, C., Saintonge, A., Brodwin, M., Dunlop, J. S., Farrah, D., Finkelstein, K. D., Finkelstein, S. L., Lotz, J., McLure, R. J., Momcheva, I., & Willmer, C. N. A. 2010, ApJ, 719, L126

van Dokkum, P. G., Förster Schreiber, N. M., Franx, M., Daddi, E., Illingworth, G. D., Labbé, I., Moorwood, A., Rix, H.-W., Röttgering, H., Rudnick, G., van der Wel, A., van der Werf, P., & van Starkenburg, L. 2003, ApJ, 587, L83

Vanden Berk, D. E., Richards, G. T., Bauer, A., Strauss, M. A., Schneider, D. P., Heckman, T. M., York, D. G., Hall, P. B., Fan, X., Knapp, G. R., Anderson, S. F., Annis, J., Bahcall, N. A., Bernardi, M., Briggs, J. W., Brinkmann, J., Brunner, R., Burles, S., Carey, L., Castander, F. J., Connolly, A. J., Crocker, J. H., Csabai, I., Doi, M., Finkbeiner, D., Friedman, S., Frieman, J. A., Fukugita, M., Gunn, J. E., Hennessy, G. S., Ivezić, Ž., Kent, S., Kunszt, P. Z., Lamb, D. Q., Leger, R. F., Long, D. C., Loveday, J., Lupton, R. H., Meiksin, A., Merelli, A., Munn, J. A., Newberg, H. J., Newcomb, M., Nichol, R. C., Owen, R., Pier, J. R., Pope, A., Rockosi, C. M., Schlegel, D. J., Siegmund, W. A., Smee, S., Snir, Y., Stoughton, C., Stubbs, C., SubbaRao, M., Szalay, A. S., Szokoly, G. P., Tremonti, C., Uomoto, A., Waddell, P., Yanny, B., & Zheng, W. 2001, AJ, 122, 549

Venemans, B. P., Kurk, J. D., Miley, G. K., Röttgering, H. J. A., van Breugel, W., Carilli, C. L., De Breuck, C., Ford, H., Heckman, T., McCarthy, P., & Pentericci, L. 2002, ApJ, 569, L11

Venemans, B. P., Röttgering, H. J. A., Miley, G. K., van Breugel, W. J. M., de Breuck, C., Kurk, J. D., Pentericci, L., Stanford, S. A., Overzier, R. A., Croft, S., & Ford, H. 2007, A&A, 461, 823

Visvanathan, N. & Sandage, A. 1977, ApJ, 216, 214

Wang, T., Elbaz, D., Daddi, E., Finoguenov, A., Liu, D., Schreiber, C., Martín, S., Strazzullo, V., Valentino, F., van der Burg, R., Zanella, A., Ciesla, L., Gobat, R., Le Brun, A., Pannella, M., Sargent, M., Shu, X., Tan, Q., Cappelluti, N., & Li, Y. 2016, ApJ, 828, 56

Wechsler, R. H., Zentner, A. R., Bullock, J. S., Kravtsov, A. V., & Allgood, B. 2006, ApJ, 652, 71

Welikala, N., Béthermin, M., Guery, D., Strandet, M., Aird, K. A., Aravena, M., Ashby, M. L. N., Bothwell, M., Beelen, A., Bleem, L. E., de Breuck, C., Brodwin, M., Carlstrom, J. E., Chapman, S. C., Crawford, T. M., Dole, H., Doré, O., Everett, W., Flores-Cacho, I., Gonzalez, A. H., González-Nuevo, J., Greve, T. R., Gullberg, B., Hezaveh, Y. D., Holder, G. P., Holzapfel, W. L., Keisler, R., Lagache, G., Ma, J., Malkan, M., Marrone, D. P., Mocanu, L. M., Montier, L., Murphy, E. J., Nesvadba, N. P. H., Omont, A., Pointecouteau, E., Puget, J. L., Reichardt, C. L., Rotermund, K. M., Scott, D., Serra, P., Spilker, J. S., Stalder, B., Stark, A. A., Story, K., Vanderlinde, K., Vieira, J. D., & Weiß, A. 2016, MNRAS, 455, 1629

White, S. D. M. & Rees, M. J. 1978, MNRAS, 183, 341

Xue, R., Lee, K.-S., Dey, A., Reddy, N., Hong, S., Prescott, M. K. M., Inami, H., Jannuzi, B. T., & Gonzalez, A. H. 2017, ApJ, 837, 172

Yang, Y., Zabludoff, A., Eisenstein, D., & Davé, R. 2010, ApJ, 719, 1654

Yang, Y., Zabludoff, A., Jahnke, K., & Davé, R. 2014, ApJ, 793, 114

Yang, Y., Zabludoff, A., Jahnke, K., Eisenstein, D., Davé, R., Shectman, S. A., & Kelson, D. D. 2011, ApJ, 735, 87

Zehavi, I., Contreras, S., Padilla, N., Smith, N. J., Baugh, C. M., & Norberg, P. 2018, ApJ, 853, 84

Zentner, A. R., Hearin, A. P., & van den Bosch, F. C. 2014, MNRAS, 443, 3044

Zheng, Z. Y., Wang, J. X., Finkelstein, S. L., Malhotra, S., Rhoads, J. E., & Finkelstein, K. D. 2010, ApJ, 718, 52

TABLE 3
Catalog of LAE candidates

ID	R.A. (J2000)	Decl. (J2000)	$\log(L_{\mathrm{Ly}\alpha})$ [erg s^{-1}]	$\log(L_{1700})$ [erg s^{-1} Hz^{-1}]	$W_{0,\mathrm{Ly}\alpha}$ [Å]	LBG*	$o3 - g$	$g - r$	$o3$	β
LAE11899†	36.331703	-4.62293	42.27±0.14	28.20±0.09	20.1±8.3	1	-1.05±0.13	0.52±0.06	24.68±0.19	-1.8±0.2
LAE31361†	36.147567	-4.34230	43.01±0.04	28.49±0.04	49.2±6.8	1	-1.65±0.06	0.29±0.04	23.11±0.07	−1.8 ± 0.4
LAE33092†	36.133734	-4.31694	42.46±0.11	28.10±0.09	35.6±12.8	1	-1.40±0.14	0.43±0.09	24.40±0.19	−2.5 ± 0.7
LAE34191†	36.112236	-4.30260	42.82±0.06	28.64±0.04	22.9±3.8	1	-1.12±0.05	0.44±0.03	23.37±0.08	−2.1 ± 0.5
QSO30046	36.461127	-4.36170	43.87±0.00	29.49±0.00	81.6±1.3	0	-1.96±0.01	1.30±0.01	21.06±0.01	−3.9 ± 0.5
LAB17139	36.082992	-4.54653	43.32±0.03	28.62±0.03	63.3±7.3	0	-1.81±0.05	0.13±0.05	22.37±0.06	−2.6 ± 0.8
LAE1223	36.548107	-4.78182	42.62±0.10	28.21±0.08	33.3±10.1	1	-1.38±0.11	0.17±0.07	23.99±0.16	−1.6 ± 0.1
LAE3003	36.544044	-4.75342	42.42±0.11	28.00±0.10	37.6±13.3	1	-1.48±0.15	0.18±0.12	24.52±0.18	−1.1 ± 0.2
LAE3007	36.347336	-4.75314	(42.03)	(27.09)	(123.3)	1	-1.65±0.19	<-0.41	25.69±0.75	(-1.7)
LAE3622	36.559838	-4.74334	42.18±0.15	27.74±0.13	44.3±22.4	1	-1.59±0.16	0.33±0.14	25.18±0.28	-1.2±0.1
LAE3833	36.399597	-4.74040	42.70±0.04	28.33±0.04	42.0±5.9	1	-1.54±0.06	0.52±0.05	23.85±0.07	-1.9±0.2
LAE4290	36.580112	-4.73362	(42.56)	(27.09)	(482.1)	0	<-4.30	−	24.49±0.11	(-1.7)
LAE4423	36.532995	-4.73160	(42.21)	(27.05)	(130.1)	1	-2.33±0.26	-0.46±0.59	25.29±0.19	(-1.7)
LAE4564	36.196192	-4.73027	42.53±0.05	27.60±0.10	95.3±21.4	0	-2.15±0.12	-0.35±0.24	24.42±0.09	-0.3±0.2
LAE4614	36.531916	-4.72931	42.38±0.10	28.15±0.09	29.6±9.7	1	-1.31±0.16	0.47±0.10	24.56±0.15	-1.3±0.5
LAE5378	36.626309	-4.71876	42.41±0.10	27.45±0.13	174.8±93.0	1	-2.51±0.21	0.24±0.24	24.78±0.22	-2.0±1.7
LAE7142	36.383586	-4.69378	42.41±0.12	28.05±0.10	35.5±13.6	1	-1.43±0.16	0.32±0.10	24.52±0.19	-1.4±0.2
LAE7560	36.517002	-4.68750	42.32±0.07	27.68±0.08	48.4±12.4	1	-1.61±0.12	0.06±0.11	24.83±0.13	-2.6±0.5
LAE8382	36.475010	-4.67657	42.77±0.04	28.35±0.04	34.4±5.0	1	-1.39±0.05	0.21±0.04	23.64±0.07	-1.9±0.1
LAE8783	36.262082	-4.67020	42.37±0.06	27.41±0.10	106.5±29.2	1	-2.21±0.14	-0.22±0.24	24.83±0.12	-1.1±0.4
LAE9355	36.224172	-4.66214	42.78±0.03	27.99±0.03	87.3±11.6	1	-2.07±0.07	0.08±0.09	23.79±0.06	-1.4±0.7
LAE9436	36.416560	-4.66001	42.11±0.13	27.28±0.17	52.5±25.1	1	-1.72±0.19	-0.52±0.32	25.38±0.25	-0.8±2.3
LAE9589	36.276072	-4.65831	42.60±0.06	27.95±0.06	48.2±10.4	1	-1.63±0.08	-0.05±0.10	24.14±0.11	-1.9±1.0
LAE9596	36.207723	-4.65882	42.79±0.04	28.27±0.02	47.1±6.4	1	-1.61±0.06	0.24±0.05	23.65±0.07	-2.0±0.2
LAE11088	36.513041	-4.63546	42.34±0.11	27.62±0.12	71.0±30.2	1	-1.89±0.18	0.28±0.17	24.97±0.22	-2.4±0.8
LAE11215	36.449218	-4.63364	42.26±0.08	27.26±0.14	167.9±81.2	1	-2.50±0.23	0.09±0.34	25.15±0.18	-1.7±2.4
LAE11424	36.531781	-4.63014	42.29±0.16	28.18±0.10	18.8±8.3	1	-1.00±0.12	0.39±0.05	24.61±0.21	-2.0±0.4
LAE11535	36.066720	-4.62925	42.89±0.07	28.87±0.06	33.1±7.8	0	-1.42±0.09	0.89±0.04	23.34±0.12	0.5±0.5
LAE11926	36.472781	-4.62227	42.31±0.07	27.60±0.10	95.7±29.5	1	-2.17±0.15	0.03±0.19	24.97±0.14	1.5±0.3
LAE12763	36.481400	-4.60974	42.72±0.04	27.87±0.05	127.9±26.0	0	-2.31±0.08	0.31±0.08	23.99±0.09	-2.2±0.3
LAE12872	36.438421	-4.60755	42.46±0.09	27.99±0.08	30.6±9.9	1	-1.29±0.12	0.19±0.08	24.53±0.17	-2.5±0.1
LAE12900	36.049683	-4.60644	42.22±0.10	27.04±0.23	227.1±206.1	1	-2.80±0.29	-0.26±0.58	25.27±0.21	-0.1±3.6
LAE13337	36.189058	-4.60115	(42.33)	(27.21)	(150.2)	1	-2.43±0.21	-0.29±0.41	24.97±0.13	(-1.7)
LAE13519	36.344731	-4.59843	42.57±0.08	28.05±0.07	46.9±12.8	1	-1.62±0.11	0.23±0.09	24.21±0.14	-1.7±0.7
LAE13642	36.256098	-4.59568	(42.16)	(27.12)	(144.9)	1	-2.40±0.25	-0.13±0.42	25.38±0.16	(-1.7)
LAE13732	36.281673	-4.59482	42.29±0.10	28.53±0.07	23.3±7.0	0	-1.16±0.13	1.39±0.04	24.70±0.14	-1.2±0.5
LAE14869	36.431008	-4.57703	42.61±0.08	28.15±0.08	48.5±14.5	1	-1.72±0.12	0.37±0.09	24.05±0.16	-1.3±0.1
LAE16775	36.263772	-4.54861	42.19±0.15	27.96±0.11	22.7±10.7	1	-1.12±0.16	0.27±0.09	24.94±0.23	-1.8±0.1
LAE17045	36.598313	-4.54491	42.43±0.06	27.63±0.09	79.5±20.9	1	-1.99±0.14	0.00±0.16	24.65±0.12	-1.7±1.2
LAE17728	36.171767	-4.53675	42.80±0.06	28.26±0.05	45.2±9.3	1	-1.57±0.07	0.22±0.05	23.62±0.11	-2.4±0.1
LAE18151	36.253813	-4.52938	42.48±0.11	28.24±0.08	21.5±7.2	1	-1.07±0.10	0.24±0.05	24.20±0.16	-2.4±0.1
LAE18455	36.221296	-4.52418	42.14±0.08	27.23±0.12	150.2±68.3	0	-2.40±0.22	0.35±0.28	25.45±0.18	-2.9±2.2
LAE18514	36.153655	-4.52340	42.27±0.10	27.76±0.11	63.5±24.7	1	-1.87±0.18	0.31±0.17	25.00±0.19	0.2±0.1
LAE19027	36.069764	-4.51725	42.65±0.05	28.06±0.05	55.7±10.0	1	-1.74±0.08	0.23±0.07	24.04±0.09	-1.7±0.1
LAE19205	36.177991	-4.51562	42.85±0.06	28.64±0.05	33.6±6.0	1	-1.39±0.07	0.64±0.05	23.41±0.10	-1.4±0.4
LAE19465	36.190375	-4.51029	42.53±0.09	28.47±0.08	70.6±22.0	0	-1.92±0.11	1.72±0.05	24.38±0.17	-1.4±0.4
LAE19469	36.103684	-4.51081	42.86±0.05	28.56±0.04	34.1±5.8	1	-1.40±0.06	0.47±0.04	23.39±0.09	-1.7±0.4
LAE19503	36.103966	-4.50951	42.53±0.06	28.22±0.06	31.7±6.9	1	-1.34±0.11	0.42±0.06	24.21±0.10	-2.0±0.4
LAE19965	36.570704	-4.50256	42.31±0.16	28.13±0.11	26.0±12.5	1	-1.22±0.13	0.48±0.06	24.69±0.25	-1.5±0.1
LAE20057	36.184999	-4.50057	(42.32)	(27.09)	(427.9)	0	-2.98±0.33	<-0.37	25.05±0.18	(-1.7)
LAE20136	36.169522	-4.49970	42.32±0.11	27.67±0.12	59.6±24.5	1	-1.79±0.16	0.11±0.16	24.87±0.22	-1.6±1.1
LAE20210	36.184859	-4.49883	42.34±0.07	27.59±0.10	96.0±31.9	1	-2.13±0.16	0.26±0.17	24.90±0.15	-1.6±1.0
LAE20309	36.272384	-4.49789	42.52±0.10	28.69±0.07	22.8±6.8	1	-1.15±0.12	1.17±0.04	24.11±0.14	-1.1±0.3
LAE20334	36.210326	-4.49665	42.30±0.12	27.76±0.11	49.3±21.0	1	-1.63±0.15	0.30±0.12	24.89±0.23	-2.3±0.3
LAE20391	36.574596	-4.49574	42.22±0.11	27.89±0.09	31.1±11.2	1	-1.32±0.15	0.35±0.09	24.97±0.18	-2.2±0.8
LAE21289	36.075996	-4.48283	42.40±0.06	27.51±0.10	114.1±37.1	1	-2.25±0.16	0.08±0.19	24.78±0.14	-1.7±0.1

TABLE 3 — *Continued*

ID	R.A. (J2000)	Decl. (J2000)	$\log(L_{\text{Ly}\alpha})$ [erg s^{-1}]	$\log(L_{1700})$ [erg s^{-1} Hz^{-1}]	$W_{0,\text{Ly}\alpha}$ [Å]	LBG*	$o3-g$	$g-r$	$o3$	β
LAE21315	36.078332	-4.48304	42.62±0.07	27.96±0.09	87.5±27.6	1	-2.09±0.14	0.34±0.14	24.19±0.15	-0.7±0.1
LAE21887	36.143396	-4.47564	42.94±0.05	28.29±0.05	102.8±20.7	1	-2.18±0.08	0.58±0.07	23.41±0.10	-1.5±1.2
LAE21996	36.137965	-4.47260	42.67±0.08	28.07±0.08	59.4±17.7	1	-1.75±0.11	0.36±0.09	24.00±0.16	-2.8±1.2
LAE22629	36.470213	-4.46346	42.34±0.09	27.93±0.08	49.0±15.7	1	-1.66±0.12	0.48±0.09	24.78±0.17	-1.3±0.8
LAE23293	36.058462	-4.45461	43.13±0.02	28.39±0.03	73.4±7.2	1	-1.94±0.04	0.09±0.04	22.88±0.05	-1.8±0.3
LAE23302	36.337272	-4.45334	42.25±0.08	27.21±0.16	132.0±60.0	0	-2.33±0.22	-0.14±0.35	25.15±0.18	-2.1±2.8
LAE23320	36.057467	-4.45327	42.37±0.09	27.52±0.13	117.0±52.2	1	-2.28±0.19	0.12±0.23	24.85±0.20	-0.9±0.1
LAE24442	36.133481	-4.43661	42.25±0.12	27.97±0.08	20.9±7.1	1	-1.04±0.13	0.10±0.07	24.75±0.15	-2.5±1.0
LAE25508	36.105297	-4.42287	42.52±0.11	28.05±0.10	59.1±23.3	1	-1.80±0.16	0.50±0.13	24.37±0.21	-1.1±0.4
LAE26131	36.476590	-4.41338	42.12±0.12	27.73±0.11	32.4±13.3	1	-1.35±0.15	0.23±0.10	25.23±0.21	-2.0±1.7
LAE26308	36.521510	-4.41145	42.31±0.13	27.24±0.19	223.7±170.5	1	-2.68±0.24	-0.04±0.41	25.06±0.30	-0.4±0.1
LAE26947	36.401936	-4.40294	42.36±0.08	27.69±0.08	38.9±10.7	1	-1.45±0.09	-0.20±0.10	24.69±0.15	-2.9±0.1
LAE28041	36.147012	-4.38820	42.61±0.10	28.29±0.08	31.2±9.6	1	-1.33±0.11	0.36±0.06	24.00±0.16	-1.9±0.5
LAE28534	36.261246	-4.38168	43.06±0.03	28.53±0.03	52.1±5.9	1	-1.70±0.05	0.25±0.04	22.99±0.06	-1.3±0.2
LAE28985	36.275809	-4.37465	42.48±0.06	27.72±0.08	76.2±20.2	1	-1.94±0.12	0.13±0.13	24.51±0.13	-2.5±1.0
LAE29112	36.574609	-4.37290	(42.50)	(27.09)	(417.3)	0	<-4.12	–	24.68±0.18	(-1.7)
LAE30621	36.335944	-4.35250	42.41±0.09	28.25±0.07	20.5±6.0	1	-1.09±0.10	0.23±0.06	24.36±0.14	-0.8±0.6
LAE31356	36.378076	-4.34067	42.46±0.08	27.72±0.11	68.3±22.5	1	-1.90±0.17	-0.01±0.20	24.55±0.15	-1.4±0.9
LAE31802	36.128128	-4.33464	(42.20)	(27.09)	(212.3)	1	<-3.45	–	25.34±0.17	(-1.7)
LAE32293	36.376859	-4.32791	42.13±0.15	28.02±0.11	24.7±11.1	0	-1.19±0.16	0.57±0.08	25.11±0.22	-1.3±0.1
LAE33330	36.425224	-4.31357	42.41±0.10	27.71±0.12	75.3±30.5	1	-1.89±0.20	0.40±0.19	24.69±0.20	-3.6±1.6
LAE34533	36.392224	-4.29760	42.56±0.07	28.02±0.07	49.0±12.5	1	-1.66±0.10	0.19±0.09	24.24±0.14	-1.4±0.6
LAE35011	36.071438	-4.28969	42.33±0.13	28.07±0.10	23.6±9.5	1	-1.15±0.14	0.22±0.07	24.60±0.19	-1.8±0.1
LAE35344	36.578088	-4.28621	42.19±0.44	27.80±0.33	49.7±68.5	1	-1.03±0.14	0.61±0.06	25.17±0.82	-1.6±0.9
LAE35637	36.360586	-4.28129	42.07±0.14	27.99±0.09	18.3±7.5	1	-0.99±0.15	0.44±0.07	25.15±0.18	-1.8±0.5
LAE35739	36.566167	-4.27998	42.39±0.11	27.93±0.11	66.0±26.6	0	-1.87±0.17	0.68±0.12	24.73±0.21	-1.4±0.4
LAE35993	36.263103	-4.27687	42.59±0.06	27.32±0.16	194.9±71.6	1	-2.59±0.16	-0.53±0.40	24.34±0.13	-1.4±0.1
LAE36621	36.504879	-4.26776	42.12±0.16	28.11±0.10	17.5±8.0	1	-0.97±0.15	0.52±0.07	25.00±0.20	-1.7±0.3
LAE36658	36.557478	-4.26803	42.55±0.08	27.54±0.14	311.4±206.0	1	-2.86±0.23	0.19±0.36	24.47±0.19	0.3±1.9
LAE37505	36.255731	-4.25733	42.22±0.13	27.81±0.10	33.9±14.1	1	-1.40±0.11	0.17±0.09	25.00±0.23	-1.5±0.3
LAE37991	36.500602	-4.25212	42.76±0.04	27.89±0.06	87.3±14.6	1	-2.05±0.09	-0.03±0.14	23.84±0.07	-2.3±0.4
LAE38096	36.625888	-4.24970	42.41±0.07	27.48±0.12	125.8±47.7	1	-2.33±0.17	-0.04±0.26	24.76±0.16	-0.8±0.3
LAE38409	36.533597	-4.24540	42.34±0.06	27.29±0.15	320.2±206.4	1	-2.86±0.26	0.27±0.41	25.00±0.14	-0.9±0.8
LAE38991	36.598963	-4.23799	42.34±0.07	27.38±0.13	108.0±36.8	1	-2.19±0.18	-0.09±0.30	24.91±0.14	-2.2±2.4
LAE40397	36.449092	-4.21805	42.17±0.14	27.79±0.11	24.7±11.0	1	-1.15±0.16	0.02±0.12	25.02±0.22	-2.4±0.9
LAE40773	36.072466	-4.21316	42.73±0.06	27.90±0.07	79.1±18.4	1	-2.01±0.09	-0.16±0.12	23.89±0.12	-0.9±1.4
LAE41503	36.088564	-4.20889	42.93±0.04	28.35±0.04	53.5±7.1	1	-1.72±0.06	0.20±0.04	23.34±0.07	-1.5±0.4
LAE42838	36.164882	-4.20061	(42.80)	(27.31)	(944.1)	1	-3.23±0.32	-0.33±0.72	23.88±0.16	(-1.7)

NOTE. — In the cases where no significant continuum flux is detected, we use 2σ flux limit for calculating the colors. For sources where there are no β measurements (i.e., at least two broad bands are not detected), we use the median β value of the other sources, and give an estimate in parentheses. For sources not detected in g, a 3σ flux limit is used to estimate the continuum flux and equivalent width.

† The spectroscopic redshifts are z=3.133, 3.124, 3.131, and 3.130 for LAE11899, LAE31361, LAE33092, and LAE34191, respectively.

* Whether this LAE also satisfies the LBG selection criteria; 1–yes, 0–no.